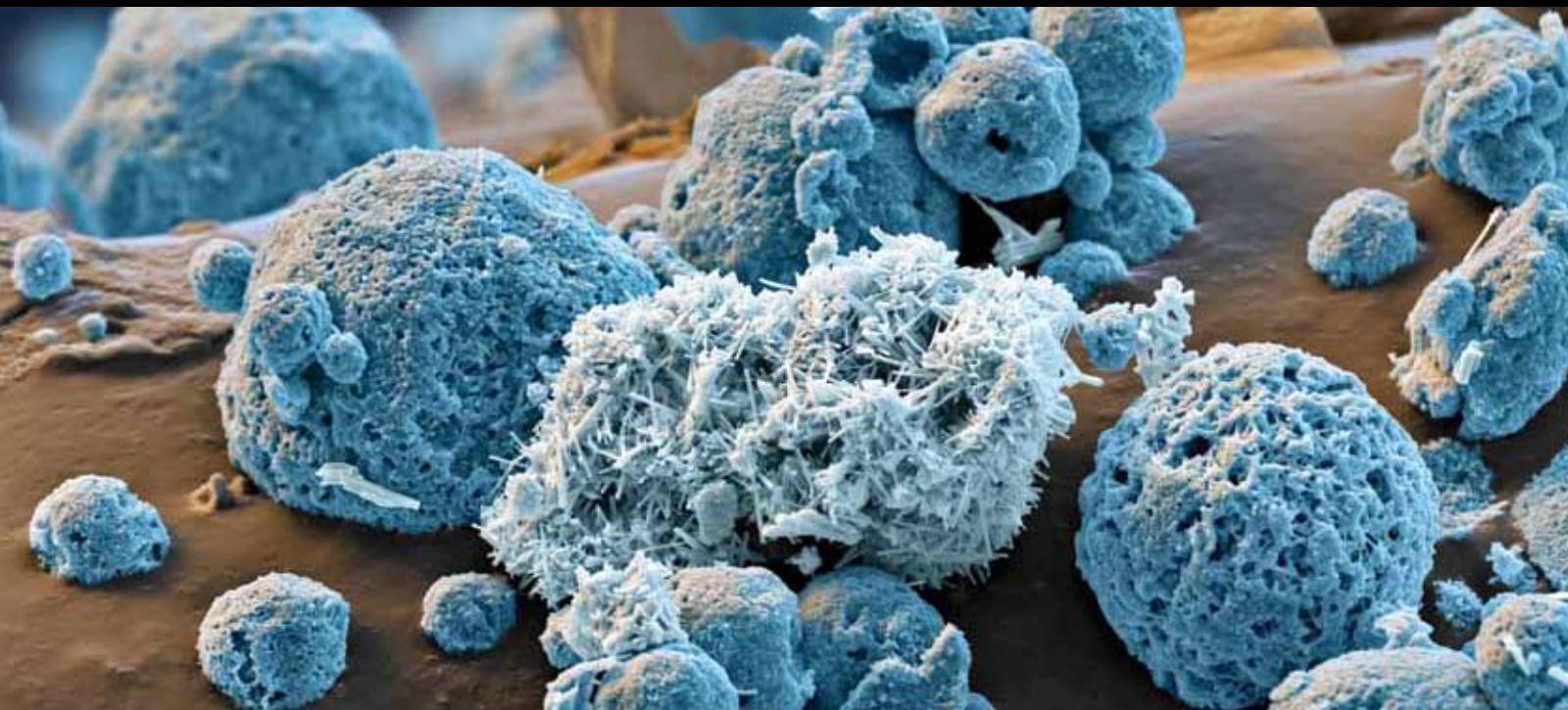


Lithium-Ion Batteries: Recent Advances and New Horizons

Guest Editors: S. Gopukumar, Duncan H. Gregory,
Hyun-Soo Kim, and Dong Shu





Lithium-Ion Batteries: Recent Advances and New Horizons

International Journal of Electrochemistry

Lithium-Ion Batteries: Recent Advances and New Horizons

Guest Editors: S. Gopukumar, Duncan H. Gregory,
Hyun-Soo Kim, and Dong Shu



Copyright © 2012 Hindawi Publishing Corporation. All rights reserved.

This is a special issue published in "International Journal of Electrochemistry." All articles are open access articles distributed under the Creative Commons Attribution License, which permits unrestricted use, distribution, and reproduction in any medium, provided the original work is properly cited.

Editorial Board

Maria Carmen Arévalo, Spain
Shen-Ming Chen, Taiwan
Abel César Chialvo, Argentina
Jean-Paul Chopart, France
A. Rodrigues de Andrade, Brazil
Sergio Ferro, Italy
Gerd-Uwe Flechsig, Germany
Rubin Gulaboski, Germany
Shengshui Hu, China
Mehran Javanbakht, Iran
Jiye Jin, Japan

Emilia Kirowa-Eisner, Israel
Boniface Kokoh, France
Emmanuel Maisonhaute, France
Grzegorz Milczarek, Poland
Valentin Mirceski, Macedonia
Mohamed Mohamedi, Canada
Angela Molina, Spain
Davood Nematollahi, Iran
K. I. Ozoemena, South Africa
María Isabel Pividori, Spain
Miloslav Pravda, Ireland

Manfred Rudolph, Germany
Benjamín R. Scharifker, Venezuela
Auro Atsushi Tanaka, Brazil
Germano Tremiliosi-Filho, Brazil
Hamilton Varela, Brazil
Jay D. Wadhawan, UK
Jose H. Zagal, Chile
Sheng S. Zhang, USA
Jiujun Zhang, Canada
Xueji Zhang, USA

Contents

Lithium-Ion Batteries: Recent Advances and New Horizons, S. Gopukumar, Duncan H. Gregory, Hyun-Soo Kim, and Dong Shu
Volume 2012, Article ID 878416, 2 pages

Quantifying Cell-to-Cell Variations in Lithium Ion Batteries, Shriram Santhanagopalan and Ralph E. White
Volume 2012, Article ID 395838, 10 pages

Preparation and Characterisation of $\text{LiFePO}_4/\text{CNT}$ Material for Li-Ion Batteries, Rushanah Mohamed, Shan Ji, and Vladimir Linkov
Volume 2011, Article ID 283491, 5 pages

A New Class of P(VdF-HFP)- CeO_2 - LiClO_4 -Based Composite Microporous Membrane Electrolytes for Li-Ion Batteries, G. Vijayakumar, S. N. Karthick, and A. Subramania
Volume 2011, Article ID 926383, 10 pages

OCV Hysteresis in Li-Ion Batteries including Two-Phase Transition Materials, Michael A. Roscher, Oliver Bohlen, and Jens Vetter
Volume 2011, Article ID 984320, 6 pages

Influence of the C/Sn Ratio on the Synthesis and Lithium Electrochemical Insertion of Tin-Supported Graphite Materials Used as Anodes for Li-Ion Batteries, Cédric Mercier, Raphaël Schneider, Patrick Willmann, and Denis Billaud
Volume 2011, Article ID 381960, 8 pages

Editorial

Lithium-Ion Batteries: Recent Advances and New Horizons

S. Gopukumar,¹ Duncan H. Gregory,² Hyun-Soo Kim,³ and Dong Shu⁴

¹ *Electrochemical Energy Systems Division, Central Electrochemical Research Institute (CSIR), Tamil Nadu, Karaikudin 630 006, India*

² *School of Chemistry, University of Glasgow, Glasgow G12 8QQ, UK*

³ *Battery Research Centre, Korea Electrotechnology Research Institute, Changwon 641-120, Republic of Korea*

⁴ *School of Chemistry and Environment, South China Normal University, Guangzhou 510006, China*

Correspondence should be addressed to S. Gopukumar, deepika_41@rediffmail.com

Received 2 February 2012; Accepted 2 February 2012

Copyright © 2012 S. Gopukumar et al. This is an open access article distributed under the Creative Commons Attribution License, which permits unrestricted use, distribution, and reproduction in any medium, provided the original work is properly cited.

The lithium-ion battery has evolved as the major power source ever since its discovery in 1991 by Sony and represents one of the major successes of materials electrochemistry. Lithium-ion batteries are becoming more and more popular in view of the multifarious applications arising from their high voltage and high power leading to light weight and smaller size cells/batteries. In view of the growing day-to-day demand for lithium-ion batteries, intensive research is being pursued globally to develop new high performing cost effective electrode and electrolyte materials and importantly without compromising on environmental issues.

This special issue contains five papers, where five papers related to cathode, anode, electrolytes, lithium-ion cell, and two-phase transition electrode materials for lithium ion batteries, respectively.

In the paper entitled “*Preparation and characterization of LiFePO₄/CNT material for lithium ion batteries*,” R. Mohamed et al. present the synthesis technique involving growth of carbon nanotubes onto the LiFePO₄ using a novel spray pyrolysis modified CVD technique. The composite cathode exhibited excellent electrochemical performances with 163 mAh/g discharge capacity with 94% cycle efficiency at a 0.1 C discharge rate in the first cycle, with a capacity fade of approximately 10% after 30 cycles.

In the paper “*Influence of the C/Sn ratio on the synthesis and lithium electrochemical insertion of tin-supported graphite materials used as anodes for Li-ion batteries*,” C. Mercier et al. present a novel composites consisting of tin particles associated to graphite prepared by chemical reduction of tin(+2) chloride by t-BuONa-activated sodium hydride in the presence of graphite. The largest tin particles associated

to graphite layers were observed for the material with a C/Sn ratio of 16. Electrodes prepared from the C/Sn = 42 material exhibit a high reversible capacity of over 470 mAhg⁻¹ up to twenty cycles with stable cyclic performances.

In the paper, “*A new class of PVdF-HFP-CeO₂-LiClO₄ based composite microporous membrane electrolytes for Li-Ion Batteries*,” G. Vijayakumar et al. present a composite microporous membranes based on Poly (vinylidene fluoride-co-hexafluoro propylene) (PVdF-co-HFP)-CeO₂ were prepared by phase inversion and preferential polymer dissolution process. As a result, a cell fabricated with PDCME in between mesocarbon microbead (MCMB) anode and LiCoO₂ cathode had better cycling performance than a cell fabricated with PICME.

In the paper “*Quantifying cell-to-cell variations in Lithium ion batteries*,” S. Santhanagopalan et al. identifies a quantitative procedure utilizing impedance spectroscopy, a commonly used tool, to determine the effects of material variability on the cell performance, to compare the relative importance of uncertainties in the component properties and to suggest a rational procedure to set quality control specifications for the various components of a cell, that will reduce cell-to-cell variability, while preventing undue requirements on uniformity that often result in excessive cost of manufacturing but have a limited impact on the cells’ performance.

In the paper “*OCV hysteresis in Li-ion batteries including two-phase transition materials*” M. A. Roscher et al. present a relation between batteries’ state-of-charge (SOC) and open-circuit-voltage (OCV) is a specific feature of electrochemical energy storage devices. As a pronounced difference remains

between the OCV after charge and discharge adjustment, obviously the hysteresis vanishes as the target SOC is adjusted with very high current rate.

*S. Gopukumar
Duncan H. Gregory
Hyun-Soo Kim
Dong Shu*

Research Article

Quantifying Cell-to-Cell Variations in Lithium Ion Batteries

Shriram Santhanagopalan¹ and Ralph E. White²

¹ National Renewable Energy Laboratory, Golden, CO 80401, USA

² University of South Carolina, Columbia, SC 29204, USA

Correspondence should be addressed to Shriram Santhanagopalan, shriram.santhanagopalan@nrel.gov

Received 26 March 2011; Accepted 4 October 2011

Academic Editor: Dong Shu

Copyright © 2012 S. Santhanagopalan and R. E. White. This is an open access article distributed under the Creative Commons Attribution License, which permits unrestricted use, distribution, and reproduction in any medium, provided the original work is properly cited.

Lithium ion batteries have conventionally been manufactured in small capacities but large volumes for consumer electronics applications. More recently, the industry has seen a surge in the individual cell capacities, as well as the number of cells used to build modules and packs. Reducing cell-to-cell and lot-to-lot variations has been identified as one of the major means to reduce the rejection rate when building the packs as well as to improve pack durability. The tight quality control measures have been passed on from the pack manufactures to the companies building the individual cells and in turn to the components. This paper identifies a quantitative procedure utilizing impedance spectroscopy, a commonly used tool, to determine the effects of material variability on the cell performance, to compare the relative importance of uncertainties in the component properties, and to suggest a rational procedure to set quality control specifications for the various components of a cell, that will reduce cell-to-cell variability, while preventing undue requirements on uniformity that often result in excessive cost of manufacturing but have a limited impact on the cells' performance.

1. Introduction

Lithium ion batteries for consumer electronics applications such as laptop computers and camcorders have been manufactured in the millions every month [1]. A typical scrap rate of a few percentages, while has been frowned upon, has not been identified as a major impediment to the use of this technology. The typical life expectation of these cells has been three years and most applications use up to six cells in a series/parallel configuration; the operating scenario for these cells has also been mild to moderate—for example, most laptop applications do not require the cells to discharge at a rate higher than 1 C (i.e., most laptops can operate for one hour or more when powered by their batteries only) and usually operate at moderate temperatures. Consequently, the quality requirements on batteries have been considerate, compared to those on other electronic components. With the advent of large format batteries for vehicle and smart-grid applications, the requirements on cell standards have grown exponentially (e.g., compare safety standards IEEE 1625 and Electric and Hybrid Vehicle Propulsion Battery System Safety Standard, SAE J2929 [2]). The size of the

individual cells has increased at least three fold; the cost to build the cells has increased with their capacities and so has the need to reduce the rejection rates. Similarly, the number of cells packaged to build modules and packs for such large applications has increased as well, and the need to ensure the longer life time (e.g., ten years for battery packs used in vehicles) and to guarantee performance under harsh operating conditions demands better uniformity among the individual cells. Standard practices in the automotive industry such as Advanced Product Quality Planning (APQP) and Production Part Approval Process (PPAP) are now typical of cell manufacturers—right from raw material purchase until product testing and acceptance of the component by the OEMs. The lithium-ion chemistry has a stringent intolerance to impurities and a high requirement for uniformity at the component level. Nevertheless, the cell manufacturing process is subtly different from the manufacturing of other electronics: for example, the various functional components such as the electrolyte and separator are usually manufactured at different locations, and these components themselves contain multiple ingredients supplied by different vendors. Quality

control has been emphasized at each stage—but rarely is there a coordinated effort to quantify variations in product specifications and how variations among the different components interact. Despite efforts by various battery manufacturers to develop in-house capabilities to produce all components at one location, limited know-how on product handling has often resulted in limited improvements. Overall, battery manufacturing has, at best, remained an art even after two decades.

The most emphasis on enhancements to batteries for transport applications today is on the cost. The missing link between the requirements for the pack and the specifications for the individual cells is currently addressed by over-sizing the battery packs. A battery electric vehicle utilizes 30–50% of the available capacity in its battery to allow for longevity of the packs as well as to ensure safe operation of the battery. Reducing the size of the battery packs has been identified as a major stepping stone for long-term viability of battery-powered vehicles. Immediate efforts in place include rigorous characterization of the packs by the end-users and the OEMs; requirements on battery performance and durability have been arrived at based on voluminous drive-cycle testing, for example. Such requirements translate to tighter quality control measures all the way down to the raw-material selection. While it is important to ensure quality of the cells, it is common knowledge that variations in some materials are naturally larger than in others, and that some properties influence the performance of the cell more than others. The allowable range of uncertainty in material properties has by and large been determined on an ad-hoc basis, sometimes demanding for higher standards than necessary, resulting in added cost of manufacturing, while in other cases, the variations in material property have not been identified as critical until after extensive design of experiment studies and/or costly field incidents. Most component manufacturers collect variability in the key properties and distribute this information to the cell manufacturers. Similarly, most cell manufacturers share information about the cell-to-cell variability limits with the OEM's. A systematic approach to relate uncertainty at the material level to the cell-to-cell variations will greatly help reduce the rejection rate of the cells and prevent undue quality requirements at the component level—both leading to significant enhancement in the performance and cost of battery packs.

In this work, we demonstrate utilizing a mathematical model in the impedance domain, the correlation between the variations in material properties, and the performance at the cell level, outlining a procedure to compare the relative importance of uncertainties in the component properties and to suggest a rational procedure to set quality control specifications for the various components of a cell. The methodology presented here can be utilized as a screening test (customizable by the cell manufacturer) to ascertain quality requirements for the various components and typically involves measuring the standard a.c. impedance response at a predetermined frequency(ies)—similar to the cell internal resistance measurement used currently in the industry.

2. Mathematical Model

The choice of impedance spectroscopy as the screening tool provides the flexibility for use without introducing significant perturbation to the cell, from the requisite operating protocol and results in minimal changes to the cell characteristics. So, this technique has been employed extensively in the past to investigate response of electrochemical systems [3]. Several mathematical models for the impedance response of lithium ion batteries exist in the literature [4–11]. Whereas the most common approach to interpreting impedance response is utilizing empirical equivalent circuits [3]; for the purpose of identifying critical material components and their relative impact on the cell performance, a physics-based model is preferable. The model developed by Darling and Newman [4] utilizes the porous electrode theory to account for the effect of parameters like porosity, particle size distribution, and thickness of the electrode as well as properties of the electrolyte on the cell impedance. This model also captures the surface effects on the kinetics as well as the dependence of the thermodynamics on the chosen chemistry. Dees et al. [6] used a similar model to characterize surface modifications on the cathode. Since then, Meyers et al. [5] and Methekar et al. [11] have developed closed-form solutions under limiting cases that allow one to interpret the physical significance of the impedance measurements at various frequencies. More recently, comprehensive models to simulate the performance of a lithium ion cell containing two intercalation electrodes and a porous separator have been developed by Sikha and White [8, 9] and Motupally et al. [12].

In the present work, we utilize the results of Sikha and White [8, 9] to simulate the impedance response of the cell. The use of this model has a few advantages: the contributions from the individual components to the overall cell impedance are readily recognizable; the closed-form transfer function for the lithium ion cell allows us to use the conventional tools [13–23] in controls theory to investigate effects of uncertainty in the parameters on the cell performance. Further details on the model equations can be found in [8, 9]. A list of base parameters used in the present work is summarized in Table 1 [9]. As discussed in subsequent sections, these parameters are perturbed to reflect the variations during the manufacturing process and their relevance to the cell performance. The cell model incorporating the base-line parameters is referred to as the “nominal” cell model in the discussion.

The cell impedance was evaluated between $1e-6$ and $1e-4$ Hz, using the closed form solution presented by Sikha, using Matlab ©. For an elaborate description of the versatility of the model and its applicability under various limiting conditions, the reader is referred to the original work; it is worth mentioning that sufficient care must be taken to ensure numerical precision as addressed in the earlier efforts [5, 9]. The entire frequency range was evenly divided in the log space into 1000 frequencies. The results shown are for a cobalt oxide cathode, a polypropylene separator, and a graphitic anode.

TABLE 1: List of nominal parameters used in the impedance model.

| Parameter | Cathode | Separator | Anode |
|---|-----------|------------|--------------|
| Diffusion coefficient in the solid particles (m^2/s) | $1e-12$ | — | $3.7125e-14$ |
| Solid phase conductivity (S/m) | 10 | | 100 |
| Nominal porosity | 0.3 | 0.45 | 0.4382 |
| Filler fraction | 0.15 | | 0.0566 |
| Transfer coefficient | 0.5 | | 0.5 |
| Nominal particle size (μm) | 8.5 | | 12.5 |
| Equilibrium exchange current density (A/m^2) | 10 | | 10 |
| Double layer capacitance for the electrode (F/m^2) | 0.2 | | 0.2 |
| Double layer capacitance for the surface film (F/m^2) | 0.02 | | 0.02 |
| Resistance for the surface film ($\text{Ohm}\cdot\text{m}^2$) | $1e-4$ | | $5e-4$ |
| Tortuosity | 2.3 | 1.5 | 4.1 |
| Nominal electrode thickness (μm) | 70 | 25 | 73.5 |
| Stoichiometric window | 0.99–0.52 | | 0.7952–0.01 |
| Initial concentration of the electrolyte (M) | | 1 | |
| Conductivity of the electrolyte (S/m) | | 10 | |
| Diffusivity in the electrolyte (m^2/s) | | $2.58e-10$ | |
| Transport number | | 0.435 | |
| Nominal room temperature | | 298 K | |

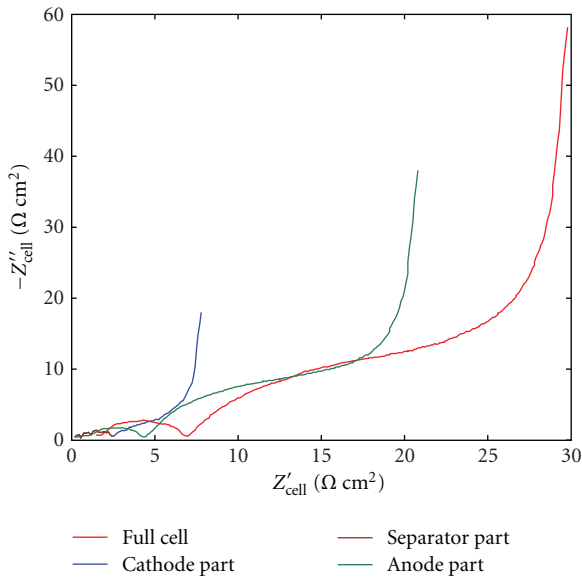


FIGURE 1: Nyquist plot showing the contribution of the individual cell components towards the overall impedance of the cell at a full cell SOC value of 0.5, between 10^6 and 10^{-4} Hz.

3. Results and Discussion

Figure 1 presents the Nyquist response for the nominal cell—the results presented are similar to the 50% state of charge (SOC) case presented by Sikha and White [9]. The model captures the low-frequency diffusion tail followed by the solution phase transport features, charge transfer, and double layer effects and finally the ohmic drop with increasing range of frequencies. Also shown is the impedance of the

individual components—namely, the anode, cathode, and the separator. For the nominal cell, the contributions from the separator were found to be negligible; the anode and cathode responses were similar in shape: each curve showing the characteristic features described above.

3.1. Incorporating Distributed Parameters. Earlier efforts to incorporate distribution in material properties, have considered model electrodes fabricated to include several characteristic particle sizes. For example, Darling and Newman [4] illustrated that the coulombic capacity of the nonuniform electrodes was consistently lower than the predictions made from a model utilizing a single particle size, at a prescribed galvanostatic discharge rate. The results were shown to progressively worsen at higher rates and with increasing particle nonuniformity. Hence, models which presume a constant particle radius were inferred to show the poorest agreement with experimental results at high discharge rates. Stephenson et al. [7] extended these results to incorporate six characteristic particle sizes. In a similar work, Nagarajan et al. [10] demonstrate that an electrode comprised of particles of two different sizes can have a significantly higher capacity than an electrode consisting of single-size particles and that a trade-off between packing density and liquid-phase diffusion resistance can be achieved by adjusting the particle size, volume fraction of large and small particles, and the size ratio to optimize discharge capacity under different operating scenario. Wang and Srinivasan [24] introduced a direct numerical simulation technique that can incorporate a continuous variation in particle size. More recently, Meyers et al. [5] implemented an impedance model that represents the particle radius using a characteristic length obtained by integrating the particle size distribution. We presented a method-

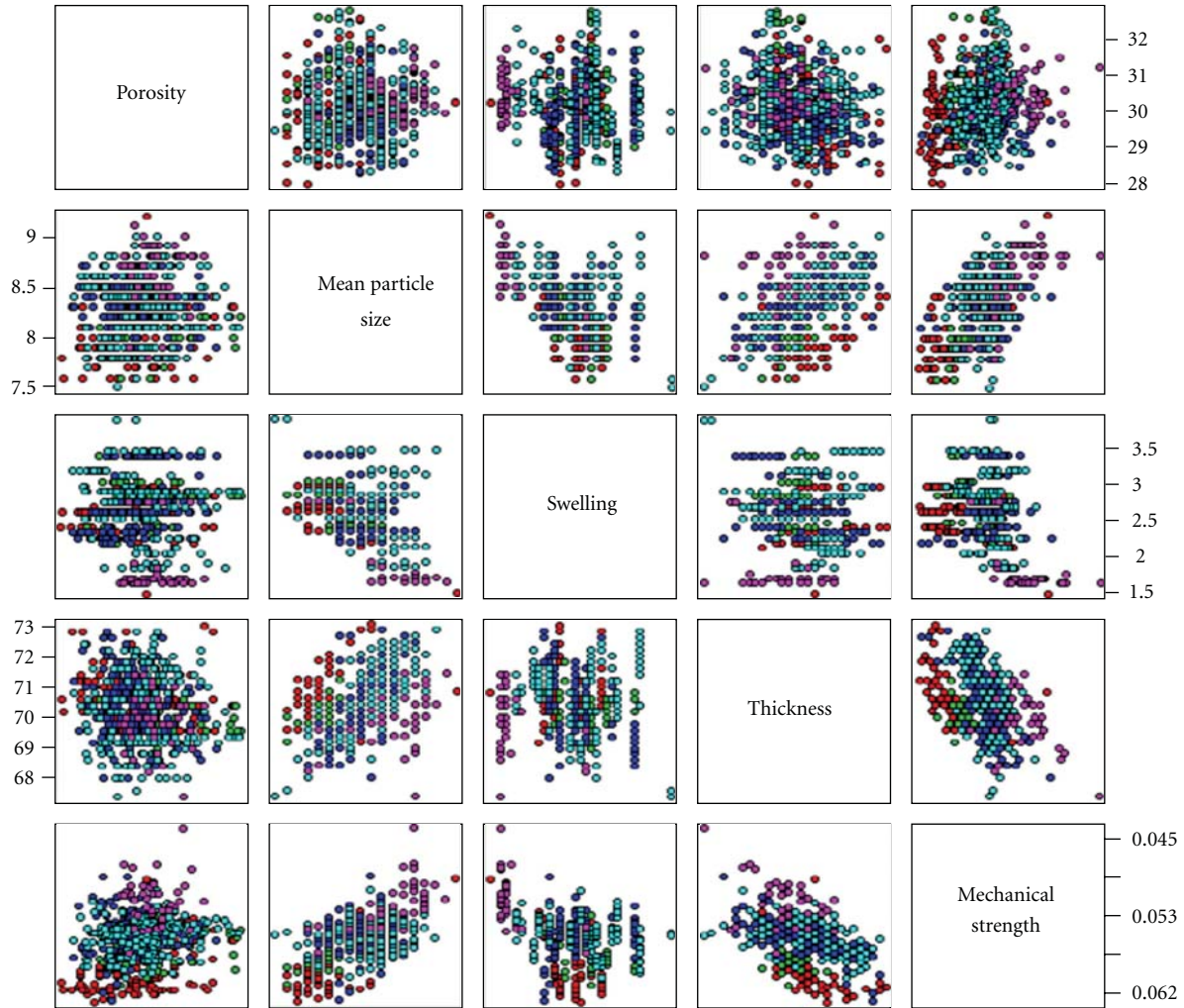


FIGURE 2: Interdependence of five battery material properties: the different colors indicate cells made from five different batches; the spread in each box shows how different the codependence of each pair of properties can be from another. For example, moving across the last column, the mechanical strength and porosity show a weaker correlation, compared to mechanical strength and thickness.

ology to incorporate distributed parameter values into simple battery models using the polynomial chaos approach [14]. However, the limitations on the complexity of the battery model did not allow for extension of the technique to applications beyond system identification. Dubarry et al. [25] analyzed the differences in cell capacity and the weight distribution in 100 cells using an equivalent circuit model and related these issues to the intrinsic cell imbalance to improve the fidelity of battery pack simulations when cell-to-cell variations were taken into consideration. The authors quantified the rate and SOC dependence of the polarization resistance in the cells to understand the effect of cell-to-cell variations on performance and at the pack level. While presenting a significant improvement over the prior work, the method presented in Dubarry's work could not be used to compare variations from one cell component versus another, largely due to the choice of a simple battery model. Other efforts include models that model nonuniformity in electrodes using Latin hypercubes for sample spacing [26] and

Kinetic Monte Carlo Simulations [11]. Very few of these models incorporate features to address the interaction of different parameters and are hence limited in their practical applicability to address cell quality.

Figure 2 shows the distribution of five different parameters and their codependence on each other. For example, these parameters, A through E, may indicate the porosity, thickness, the mean particle-size, swelling, and mechanical strength of the electrode respectively. The different colors indicate different batches of the product. Two observations are apparent from the data: (i) the parameters specified by the manufacturer to characterize a component are interdependent on each other and (ii) the dependence of a given parameter (e.g., Mechanical Strength) upon one property (e.g., Mean Particle Size) is drastically different from that on another (e.g., Thickness). Failure to comprehend these results often leads to design of experiments focused on optimizing parameters one at a time and does not lead to fruition. In the next few sections, we present a methodology to

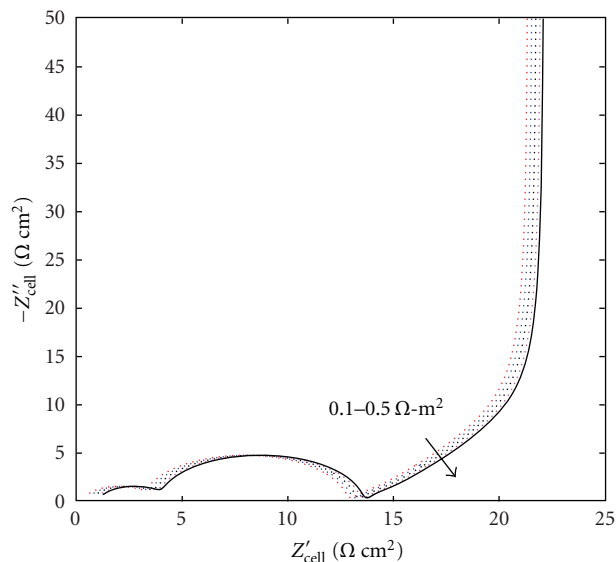


FIGURE 3: Effect of contact resistance on the impedance response of the cathode: the incorporation of an ohmic drop across the terminals shifts the real axis of the nominal response to more positive values.

incorporate such statistical information obtained in the industry to analyze the relative impact of the different parameters on the cell performance.

3.2. Sensitivity Analysis. As mentioned earlier, the advantage of frequency domain analysis is the ability to capture the signature of phenomena exhibiting different time constants using small perturbations about the equilibrium state. According to the difference in the response time, ohmic drop and kinetic processes are often found to alter the high frequency response, while the effect of slower transport processes is observed at the lower frequencies, around the diffusion tail. It is a standard practice to carry out sensitivity analyses to understand the effect of the different parameters. Figure 3 shows the effect of the contact resistance on the impedance response of the cathode, for example, the incorporation of an ohmic drop across the terminals merely shifts the real axis of the nominal response to more positive values. This is a relatively simple result to interpret, both since the resistive component does not have an imaginary component part and because the time constant for a resistor is significantly different from the other processes taking place within the cell.

Figure 4 presents the interaction of the distribution in different parameter values. Four different parameters are chosen for analysis: the cathode thickness, porosity, tortuosity, and the mean particle radius for the cathode. Note that the particle size is represented by a single value in the model by Sikha and White [8]; however, extension to the equivalent characteristic length approach presented by Meyers et al. [5] to include particle size distributions, is straight forward. In each case, the parameter of interest is perturbed from the nominal value shown in Table 1 by the range indicated in the corresponding Figures Figure 4(a) through 4(d) while retaining the other parameters at their

nominal values. Note that the range across which the properties are altered is within the range of experimental variations. Some of these parameters have a greater influence on the impedance response, compared to the others; this trend reflects the choice of nominal values for the parameters chosen and should not be interpreted as the norm. Also, whereas some of the parameters are readily controlled during the manufacturing process, others are usually measured at a later stage to ensure quality requirements—for example, the tortuosity is not preset to a specific value; it is measured after the electrode is fabricated to account for a certain loading, particle size, and thickness. Nevertheless, the effect of tortuosity is independent of that of the other parameters and is significant under the conditions shown in Figure 4. Typically in such cases, the parameter of interest (here, the tortuosity) has a broader distribution than those that can be preset.

Figure 5 compares the effect of variations in similar parameters (thickness, porosity, and tortuosity) between the separator and the cathode. Since changes in these properties both in the cathode as well as in the separator alter transport in the electrolyte, the low medium frequency (e.g., ~ 1 mHz) response reflects these perturbations for all cases. It is under situations like these, when there is an overlap in the response, that a physics-based model is valuable to directly correlate the changes in the design parameters within a meaningful range to the variations in the cell performance. As the results indicate, variations in the cathode, in general, have a greater impact than the corresponding changes in the separator, again, for the set of nominal parameters shown in Table 1. However, most of these values are close to actual properties measured from a working cell, and hence, the trend shown in Figures 4 and 5 is in good qualitative agreement with actual measurements, even if not rigorously quantitative. In practice, tuning the properties of one component may not be as flexible as another—for example, it is easier to fabricate thin ($10\ \mu\text{m}$) copper foils of uniform thickness since the processing limitations on metallic rolls have been overcome to a greater extent, than when fabricating composite electrodes or polymer membranes of similar thickness. In such cases, imposing the same tolerance limits for the various components results in additional cost due to increase in rejection rate as well as sophistication in material handling. However, as noted from Figure 5, such variations may not be the limiting factors that impact on the performance of the given cell design. In such instances, the overspecification of component requirements only leads to additional cost, without any noticeable impact on quality.

Despite similar results illustrated in the literature, such practices continue in the industry, primarily because of the influence of one parameter on the other, as previously discussed in Figure 2. For example, whereas the separator porosity may not be critical for a given choice of cathodes (e.g., a high energy cell), the use of a similar product for a high rate application, or even in the same cell when operated at a different temperature, may alter the sensitivity plots shown in Figures 4 and 5. In the next section, we present a methodology to compare the relative significance of the variations introduced due to the uncertainty in the different

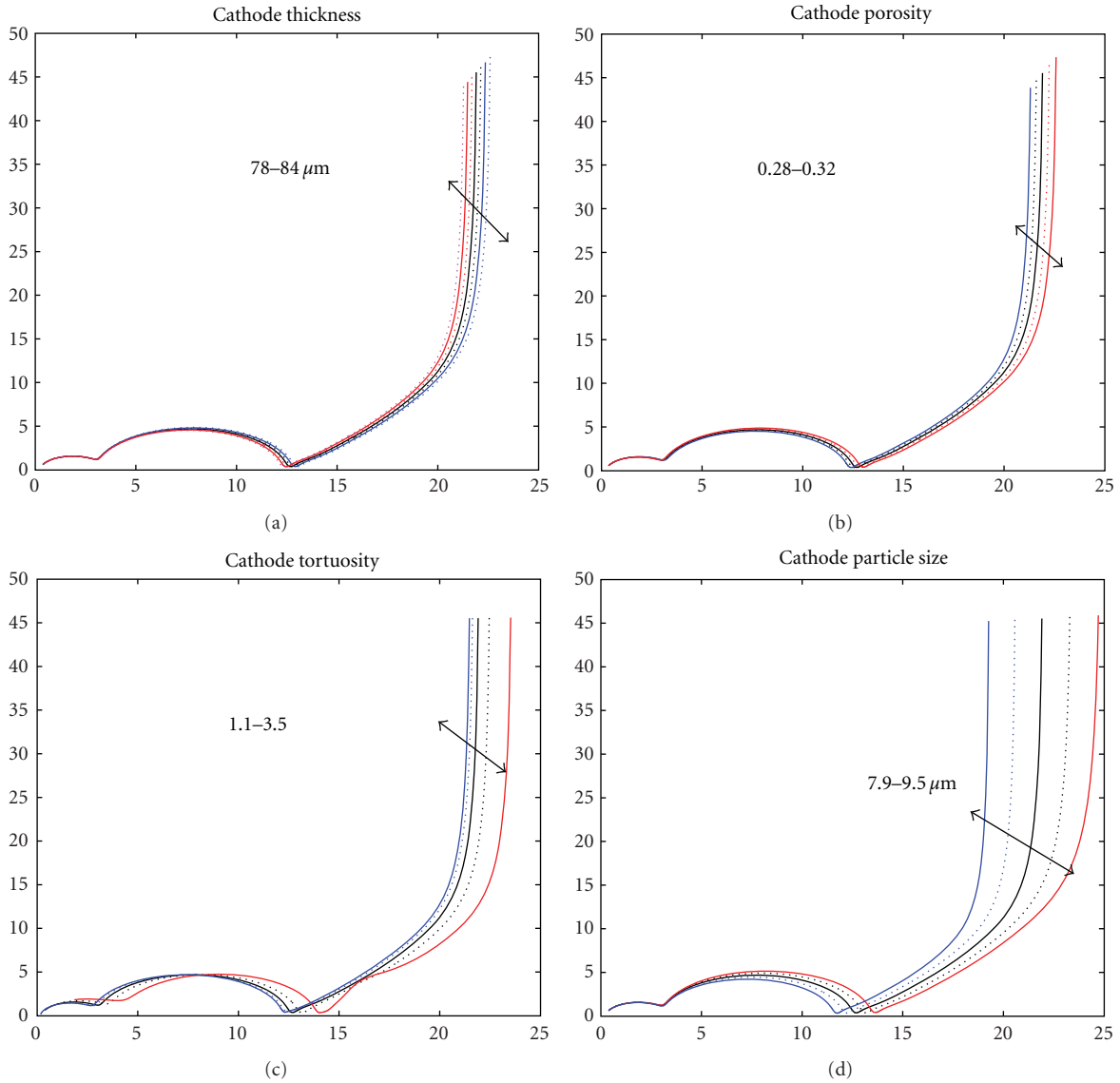


FIGURE 4: Sensitivity analysis on the cathode: plotted are the Nyquist responses when the design parameters at the cathode are swept about their corresponding nominal values, within the range of manufacturing variability.

parameters to quantify the net impact on the cell as well as to identify the best design solution available to minimize the variations in cell performance.

3.3. Parameter Uncertainty and Process Variability. Most of the discussion presented in this section draws from the literature on robust design under model uncertainties [13–23]. Extensive studies to minimize the effect of uncertainty in the input parameters on the robustness of plant performance have been carried out over several decades [13]. Box converted the correlation matrix into a diagonal form and used the eigenvalues and eigenvectors to define a hyperdimensional ellipse that represents the joint confidence intervals. Routh and Nyquist stability criteria are outlined in standard controls textbooks [15, 23]. Skogestad and Morari [16] provide a detailed mathematical framework for

handling uncertainty, and robust stability in multiple, input multiple, output (MIMO) systems introduced a formulation for design under uncertainty in input parameters, which utilizes a smooth nonlinear program that approximates the feasibility problem. Androulakis et al. [19] investigated the effect of uncertainty in the microscopic reaction rate constants on macroscopic observables such as autoignition delay. Samsatli [20] introduced a robustness metric for optimization under parametric uncertainty. Using a similar example, Skogestad and Morari [16] compare the differences between the use of SSV's for SISO and MIMO systems and present an extension of the Nyquist stability criterion for MIMO systems. This approach will be used in the rest of the current work. In essence, this approach utilizes the Nyquist plots shown in Figures 4 and 5 to capture the impact of parametric uncertainty on the performance of the system. Figure 6(a) focuses on the response at 1 mHz when several

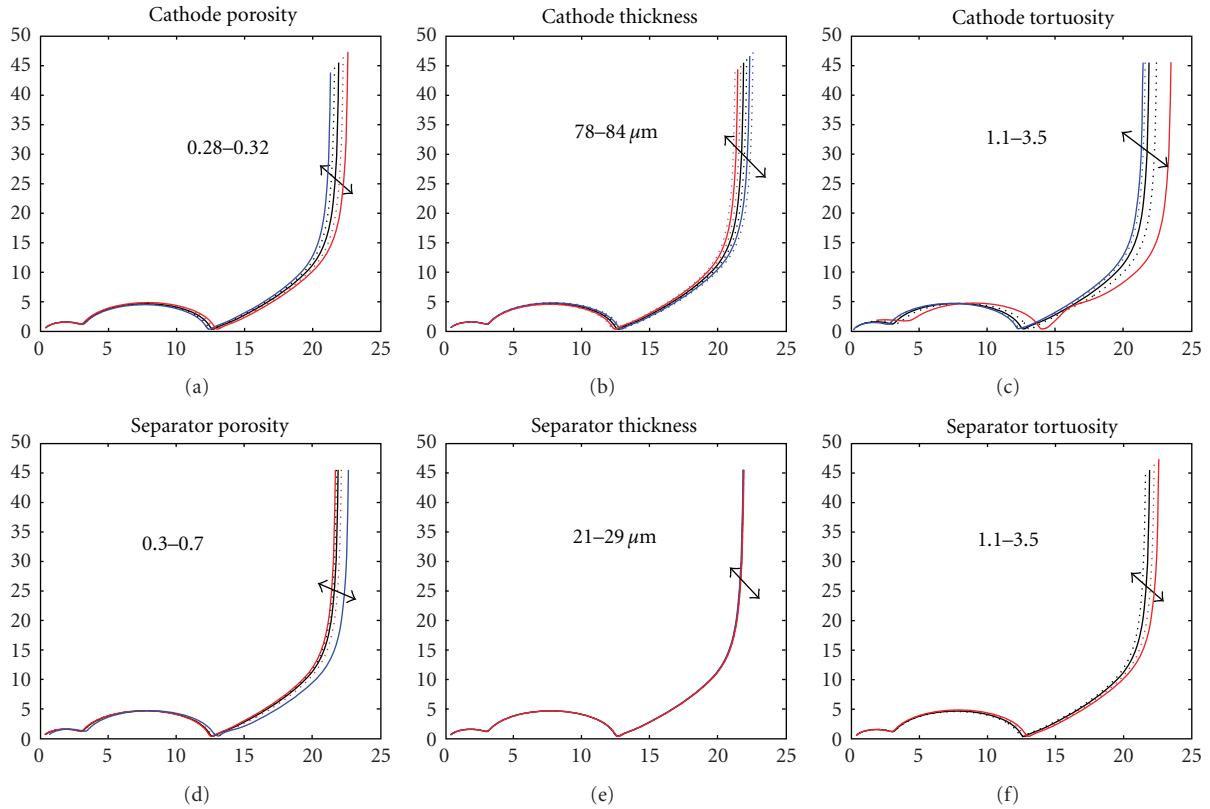


FIGURE 5: Comparison of the sensitivity of the cell impedance to the corresponding design parameters within the cathode versus the separator; for the choice of nominal parameters shown in Table 1, the variations on the separator do not impact the cell performance as much as those of the cathode.

parameters like the cathode porosity, particle size, and thickness are perturbed; these are results super-imposed from Figure 4. The method proposed by Skogestad then approximates the uncertainty in the response by a disc whose radius spans the uncertainty in the input space. Corresponding to each of the parameters shown in the figure, there exists a separate disc-approximation, as shown in Figure 6(b). In practice, the discs may not be circles for all cases; however, identifying the shape of the actual uncertain region in the response space can be a cumbersome task for the case with multiple parameters, and the methodology shown in the figure is a good approximation. The use of the individual disc-approximation corresponds to the design of experiments optimizing one parameter at a time as described in the previous sections. In the case shown in Figure 6, for example, the use of individual circles to optimize performance represents adjusting the porosity distribution, particle sizes, and variations in electrode thickness, one at a time. In practice, these parameters can be tuned individually to accomplish different goals, changing one of these parameters often leads to a change in the others—making the tuning process more complicated than that for an SISO system. The worst case scenario is represented by the circumcircle of the individual confidence regions. The best possible scenario for a given set of parameters connects the centers of the confidence discs; for this case, there is no uncertainty in the value of

any parameter; that is, each parameter is held at its nominal value and the impedance response collapses to a point value as well.

The representation of the uncertainty from the various parameters simultaneously, as shown in Figure 6, has several advantages. To begin with, one can readily see that the sensitivity of the circumcircle to the various parameters is a function of the nominal values for the parameters as well as the frequency of choice. In other words, the individual sensitivities shown in Figures 4 and 5 can now be compared against one another, by choosing an appropriate frequency. In the example shown in Figure 6, the particle size has the largest impact (i.e., the disc corresponding to that parameter has the largest diameter) on the fluctuations in the impedance, and variations in the thickness of the electrode may be masked by those in the particle size distribution within the scope of the electrochemical model used in this study. Subsequently, any effort to improve the thickness of the electrode will not lead to fruition, until the variations in the particle size are addressed for the nominal values of parameters used here. Secondly, comparison of the effect of variations in the individual parameters provides an easy-to-use metric as opposed to the variations themselves; it reduces the need for arbitrary specifications on the individual parameters or that for an extensive design of experiments, since one measure (here the cell impedance at a preset frequency) is used to

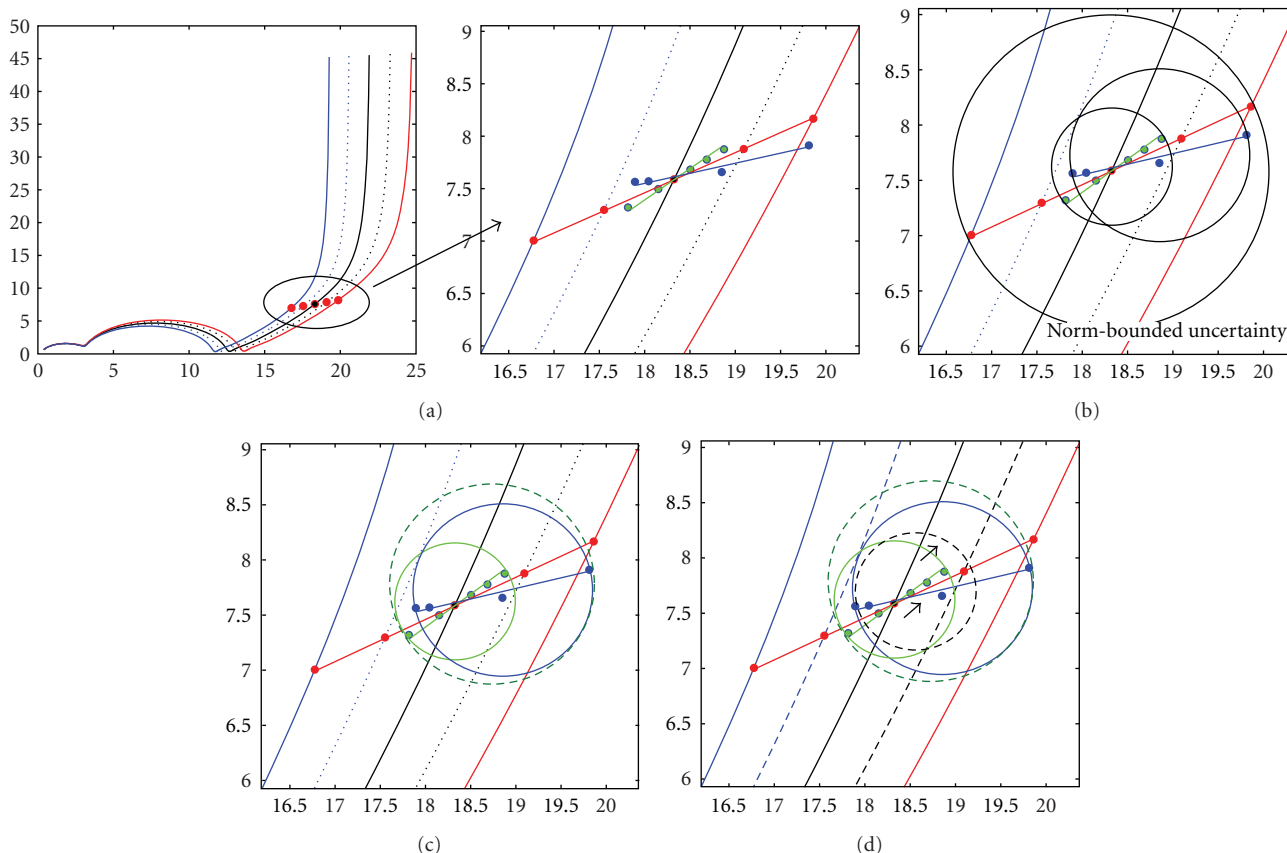


FIGURE 6: (a) Superimposing sensitivity data from Figures 4 and 5. (b) Construction of the norm-bounded uncertainties for the individual parameters: the smallest disc corresponds to the uncertainty in the cathode thickness, the medium-sized disc to that of the cathode porosity, and the largest to the particle size within the cathode. (c) Determining the overall uncertainty in the impedance response at 1 mHz: the dashed circumcircle shows the uncertainty region covering the influence of the variations in the individual parameters. (d) Setting the nominal value for the cathode thickness at $75 \mu\text{m}$ instead of $70 \mu\text{m}$ moves the individual uncertainty disc from the solid circle shown in (c) to the dotted circle, and the overall uncertainty from the dashed circumcircle to coincide with the individual disc corresponding to that of the porosity variations.

assess the impact of variations in each parameter. All efforts to minimize the cell-to-cell variations are in essence attempts to minimize the radius of the circumcircle shown in Figure 6. The obvious path forward, is to minimize the variations in the individual parameters; however, it is not always economical to tune each parameter to the desired level of uniformity. One typical example is the thickness of the current collectors versus that of the active material or the separator described in the previous section. In this case, an alternate choice of the nominal values for the different parameters may help in reducing the impact of variations in the parameter that is more difficult to tune. For instance, adjusting the nominal value for the separator thickness such that any variation on this parameter falls within the observable range of impedance variations due to the other parameters will greatly reduce the efforts that may otherwise go towards unachievable thickness uniformity improvements on a $25 \mu\text{m}$ thin polymer film, to bring it at par with a $25 \mu\text{m}$ aluminum foil. Figure 6(d) shows another example of this approach, where two parameters (the thickness and porosity of the cathode) are considered; for the nominal values used, the two

small discs shown in Figure 6(a) represent the variability in the cell impedance. However, shifting the nominal thickness of the cathode by $5 \mu\text{m}$ effectively moves the uncertainty due to the thickness into the range corresponding to that from the porosity.

In essence, we propose the following steps to translate requirements on cell-to-cell uniformity to tolerance specifications for the component manufacturers: (i) obtain the acceptable range of impedance values for the cells from different lots based on the end-user requirements, operating conditions, and so forth, (ii) use this range as the diameter for the circumcircle described in Figure 6, (iii) obtain the experimentally measured distributions in the values of the properties of interest in the different components (anode, foil, separator, electrolyte, etc.) to construct the individual confidence intervals, and (iv) match the variations in the components to accommodate all the subcircles within the acceptable range of impedance values as given by the circumcircle.

The choice of frequency domain for such analysis is based on the ease of detecting the sensitivity of the response to

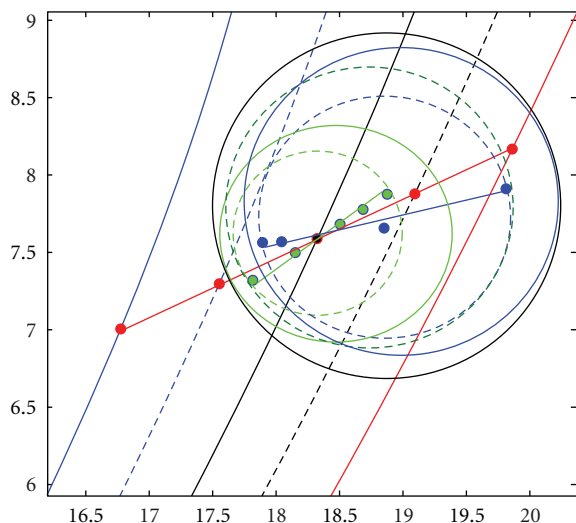


FIGURE 7: Effect of temperature on the sensitivity of the impedance response to cathode thickness and porosity: the dotted circles correspond to the uncertainties at room temperature (298 K) and the solid circles correspond to equivalent values at low temperature (263 K).

changes in the different parameters. A similar procedure using time-domain data (e.g., discharge curves) can be developed; however, it is usually difficult to distinguish experimental noise from subtle changes due to variations in the parameters. Hence, the time domain data do not reveal such trends until after prolonged use of the battery. A second advantage is the possibility of identifying a range of frequencies depending on the time constants, for the choice of parameters investigated. Also, the conventional tools used in stability analyses and robust design [13–23] can be readily extended to battery design, by posing the deviations out of the prespecified tolerance limit as being thrust into an unstable region.

3.4. Parameter Tuning Based on Operating Conditions. The previous subsections illustrate how the different parameters influence the variations within the cell to different extents. A lot of these variations also depend on the operating conditions the battery is subjected to. Figure 7 illustrates the effect of variations in the same set of parameters shown in Figure 6 at a lower temperature. As reported in the literature, the transport properties of the electrolyte are very different from those at room temperature. As a result, the sensitivity of the cell impedance to parameters like the porosity and tortuosity of the electrode is increased, and the uncertainty in the cell impedance is magnified. As seen in Figure 7, the effect of the cathode porosity is comparable with the particle-size effects when the battery is operated at low temperatures. Hence if the battery operates for a majority of the time at lower temperatures, tailoring the design to accommodate this finding will lead to addressing low temperature limitations better.

4. Summary

Cell-to-cell variations are often attributed to uncertainties in the design parameters for the different cell components. Knowing the sensitivity of the cell performance to the parameters of interest helps battery manufacturers to focus on the right set of steps, instead of enforcing ad-hoc criteria on the tolerances for different properties at quality check. A methodology was presented to facilitate studying the relative effects of multiple parameters simultaneously and to prioritize testing procedure during design of experiment studies. The process outlined above may be used to check if the individual cells from different lots conform to a prespecified tolerance limit for the battery, by measuring the scatter in the a.c. impedance of the cells at a suitable frequency. Finally, the simulation results for the different operating conditions will help tailor the design parameters according to the targeted end use. A few open questions remain: the results presented here depend entirely on the model of choice; no allowance has been provided in this work to accommodate for unmodeled dynamics. There are accounts of representing such instances as uncertainties as well; however, in most practical instances, it is hard to distinguish between variations in the parameters and those from under represented physical phenomena. A rigorous procedure to determine the “optimal” frequency at which the sensitivity analysis should be carried out has not been developed yet, for the case with uncertain parameters. The approximation of the uncertain region by discs as discussed earlier has been questioned by Bequette [2], since this approach amplifies the actual margin of discrepancy and introduces purely hypothetical scenarios in some cases. Physics-based definition of uncertainties has been recommended instead; however, the implementation requires a rigorous formulation, hence, we did not adopt this approach here. However, this idea warrants further exploration in subsequent analyses.

References

- [1] D. Linden and T. B. Reddy, Eds., *Handbook of Batteries*, 3rd edition, 2003.
- [2] Electric and Hybrid Vehicle Propulsion Battery System Safety Standard, SAE J2929.
- [3] E. Barsoukov and J. R. McDonald, Eds., *Impedance Spectroscopy: Theory, Experiment, and Applications*, Wiley-Interscience, Hoboken, NJ, USA, 2nd edition, 2005.
- [4] R. Darling and J. Newman, “Modeling a porous intercalation electrode with two characteristic particle sizes,” *Journal of the Electrochemical Society*, vol. 144, no. 12, pp. 4201–4208, 1997.
- [5] J. P. Meyers, M. Doyle, R. M. Darling, and J. Newman, “Impedance response of a porous electrode composed of intercalation particles,” *Journal of the Electrochemical Society*, vol. 147, no. 8, pp. 2930–2940, 2000.
- [6] D. Dees, E. Gunen, D. Abraham, A. Jansen, and J. Prakash, “Alternating current impedance electrochemical modeling of lithium-ion positive electrodes,” *Journal of the Electrochemical Society*, vol. 152, no. 7, pp. A1409–A1417, 2005.
- [7] D. E. Stephenson, E. M. Hartman, J. N. Harb, and D. R. Wheeler, “Modeling of particle-particle interactions in porous cathodes for lithium-ion batteries,” *Journal of the Electrochemical Society*, vol. 154, no. 12, pp. A1146–A1155, 2007.

- [8] G. Sikha and R. E. White, "Analytical expression for the impedance response of an insertion electrode cell," *Journal of the Electrochemical Society*, vol. 154, no. 1, pp. A43–A54, 2007.
- [9] G. Sikha and R. E. White, "Analytical expression for the impedance response for a lithium-ion cell," *Journal of the Electrochemical Society*, vol. 155, no. 12, pp. A893–A902, 2008.
- [10] G. S. Nagarajan, J. W. Van Zee, and R. M. Spotnitz, "A mathematical model for intercalation electrode behavior: I. Effect of particle-size distribution on discharge capacity," *Journal of the Electrochemical Society*, vol. 145, no. 3, pp. 771–779, 1998.
- [11] R. N. Methkar, P. W. C. Northrop, K. Chen, R. D. Braatz, and V. R. Subramanian, "Kinetic Monte Carlo simulation of surface heterogeneity in graphite anodes for lithium-ion batteries: passive layer formation," *Journal of The Electrochemical Society*, vol. 158, pp. A363–A368, 2011.
- [12] S. Motupally, C. C. Streinz, and J. W. Weidner, "Proton diffusion in nickel hydroxide films measurement of the diffusion coefficient as a function of state of charge," *Journal of the Electrochemical Society*, vol. 142, no. 5, pp. 1401–1408, 1995.
- [13] G. E. P. Box, "Fitting empirical data," *Annals of the New York Academy of Sciences*, vol. 86, pp. 792–794, 1960.
- [14] S. Santhanagopalan and R. E. White, "Modeling parametric uncertainty using polynomial chaos theory," *ECS Transactions*, vol. 3, no. 27, pp. 243–256, 2007.
- [15] W. L. Luyben, *Process Modeling, Simulation and Control for Chemical Engineers*, McGraw-Hill, New York, NY, USA, 2nd edition, 1989.
- [16] S. Skogestad and M. Morari, "Model uncertainty, process design, and process control," in *Proceedings of the AIChE Annual Meeting*, Chicago, Ill, USA, November, 1985.
- [17] S. Skogestad and I. Postlethwaite, *Multivariable Feedback Control: Analysis and Design*, John Wiley & Sons, West Sussex, UK, 2nd edition, 2005.
- [18] W. C. Rooney and L. T. Biegler, "Optimal process design with model parameter uncertainty and process variability," *AIChE Journal*, vol. 49, no. 2, pp. 438–449, 2003.
- [19] I. P. Androulakis, J. M. Grenda, T. A. Barckholtz, and J. W. Bozzelli, "Propagation of uncertainty in chemically activated systems," *AIChE Journal*, vol. 52, no. 9, pp. 3246–3256, 2006.
- [20] N. J. Samsatli, L. G. Papageorgiou, and N. Shah, "Robustness metrics for dynamic optimization models under parameter uncertainty," *AIChE Journal*, vol. 44, no. 9, pp. 1993–2006, 1998.
- [21] S. Balakrishnan, P. Georgopoulos, I. Banerjee, and M. Ierapetritou, "Uncertainty considerations for describing complex reaction systems," *AIChE Journal*, vol. 48, no. 12, pp. 2875–2889, 2002.
- [22] K. A. McDonald, A. Palazoglu, and B. W. Beuette, "Impact of model uncertainty descriptions for high-purity distillation control," *AIChE Journal*, vol. 34, no. 12, pp. 1996–2004, 1988.
- [23] B. A. Ogunnaike and W. H. Ray, *Process Dynamics, Modeling, and Control (Topics in Chemical Engineering)*, Oxford University Press, Cambridge, Mass, USA, 1994.
- [24] C. Y. Wang and V. Srinivasan, "Computational battery dynamics (CBD)—electrochemical/thermal coupled modeling and multi-scale modeling," *Journal of Power Sources*, vol. 110, no. 2, pp. 364–376, 2002.
- [25] M. Dubarry, N. Vuillaume, and B. Y. Liaw, "From single cell model to battery pack simulation for Li-ion batteries," *Journal of Power Sources*, vol. 186, no. 2, pp. 500–507, 2009.
- [26] Y.-B. Yi, C.-W. Wang, and A. M. Sastry, "Two-dimensional vs. three-dimensional clustering and percolation in fields of overlapping ellipsoids," *Journal of the Electrochemical Society*, vol. 151, no. 8, pp. A1292–A1300, 2004.

Research Article

Preparation and Characterisation of LiFePO₄/CNT Material for Li-Ion Batteries

Rushanah Mohamed, Shan Ji, and Vladimir Linkov

SAIAMC, University of the Western Cape, Cape Town 7535, South Africa

Correspondence should be addressed to Shan Ji, sji@uwc.ac.za

Received 23 February 2011; Revised 10 July 2011; Accepted 25 July 2011

Academic Editor: S. Gopukumar

Copyright © 2011 Rushanah Mohamed et al. This is an open access article distributed under the Creative Commons Attribution License, which permits unrestricted use, distribution, and reproduction in any medium, provided the original work is properly cited.

Li-ion battery cathode materials were synthesised via a mechanical activation and thermal treatment process and systematically studied. LiFePO₄/CNT composite cathode materials were successfully prepared from LiFePO₄ material. The synthesis technique involved growth of carbon nanotubes onto the LiFePO₄ using a novel spray pyrolysis-modified CVD technique. The technique yielded LiFePO₄/CNT composite cathode material displaying good electrochemical activity. The composite cathode exhibited excellent electrochemical performances with 163 mAh/g discharge capacity with 94% cycle efficiency at a 0.1 C discharge rate in the first cycle, with a capacity fade of approximately 10% after 30 cycles. The results indicate that carbon nanotube addition can enable LiFePO₄ to display a higher discharge capacity at a fast rate with high efficiency. The research is of potential interest for the application of carbon nanotubes as a new conducting additive in cathode preparation and for the development of high-power Li-ion batteries for hybrid electric vehicles.

1. Introduction

The exponential growth in portable electronic devices such as cellular phones and laptop computers in recent years has resulted in an enormous demand for compact and light-weight rechargeable batteries which can offer high energy densities. In addition, growing environmental concerns have simultaneously driven the development of advanced batteries for electric vehicles. Li-ion batteries are appealing candidates for these applications as they provide higher energy density compared to the other rechargeable batteries systems available, such as the lead acid, nickel cadmium (NiCd), and nickel-metal hydride (NiMH) batteries. Today, the Li-ion is the fastest growing and most promising rechargeable battery chemistry. The electrochemical performance of Li-ion batteries relies significantly on the properties of the cathode-materials, the anode materials, and the electrolytes. Carbon-based materials have been the material of choice for lithium storage in Li-ion batteries for some time [1, 2]. This paper focuses on our study of the development of new cathode materials which encompass carbon nanotubes (CNTs) to ideally produce highly specific capacities. LiFePO₄

has been reported to be an excellent cathode, but its high resistance limits the obtainable capacity. Recently, a variety of techniques have been attempted for the synthesis of high-performance LiFePO₄ [3, 4]. Mechanical activation, which involves the blending of ingredients by high-energy ball milling followed by thermal treatment at high temperature, has turned out to be a versatile technique with high capability for scale up [5, 6]. In this study, LiFePO₄/CNT composite cathode material has been synthesized via a novel synthesis technique and studied.

2. Experimental and Characterization

2.1. Experimental. LiFePO₄/CNT composite material was synthesised by growing carbon nanotubes onto LiFePO₄, via CVD using spray pyrolysis. Table 1 lists the experimental parameters employed in the CVD using spray pyrolysis technique.

LiFePO₄ material synthesised previously was placed into a quartz crucible and placed into a horizontal tube furnace. The furnace was then heated to 800°C under argon flow of

TABLE 1: Parameters employed for carbon nanotube growth via CVD using spray pyrolysis.

| | |
|-------------------------|--|
| Flushing gas | Argon (UHP) obtained from Afrox |
| Carbon source | Ethylene Gas (UHP) obtained from Afrox |
| Deposition temperatures | 800°C |
| Flushing gas flow rate | 100 ml/min |
| Carbon source flow rate | 100 ml/min |
| Times of deposition | 30, 60, 90 minutes |
| Catalyst solutions | 1.0 M NiSO ₄ |

100 ml/min. Once the set temperature was reached, a Ni mist was introduced to a tubular furnace apparatus. The mist was produced from a 1.0 M NiSO₄ solution. The argon gas flow was turned off, and ethylene gas was introduced into the furnace at a flow rate of 100 ml/min each for the desired deposition time. After the time elapsed, the final product was cooled to room temperature under an argon atmosphere.

2.2. Morphological and Structural Analysis. SEM measurements were done using a Hitachi ×650 microscope. The microscope beam energy can be varied over the range from 5 to 40 KeV, with a maximum resolution of 10 nm. Transmission electron microscopy (TEM) analyses were done using a Tecnai G2 F20 X-Twin Mat FEG-TEM. X-ray diffraction (XRD) analyses were performed using a Bruker multipurpose powder diffractometer (D8 Advance). In this investigation, the surface area and porosity of the LiFePO₄/CNT cathode materials were investigated with high sensitivity using an accelerated surface area and porosity analyser (Micromeritics ASAP 2010).

2.3. Charge/Discharge Cycle Testing. The positive electrode consisted of 80% of the as-prepared composite, 15% acetylene black, and 5% polytetrafluoroethylene (PTFE) as a binder, and Al metal was used as the current collector. The electrolyte solution was 1.0 mol·L⁻¹ LiPF₆ in EC + DMC (1 : 1). Lithium metal foil was used as the counter electrode during electrochemical measurements. All cells were assembled in an argon-filled glovebox. Charge/discharge tests were carried out using a Land-BTL10 fully automatic program test instrument. For the novel Li-ion battery cathodes synthesised, tests were run at a voltage range of 2.40 to 4.10 V versus Li/Li⁺.

2.4. Electrochemical Conductivity. Electrochemical conductivity was calculated from the resistance values obtained from impedance measurements. Electrochemical impedance spectroscopy (EIS) measurements were carried out using an Eco Chemie Autolab PGSTAT 30. The amplitude of the AC signal was 5 mV over the frequency range between 100 kHz and 0.01 Hz.

3. Results and Discussion

Figure 1 illustrates the SEM images of LiFePO₄/CNT composite cathode materials synthesised. From these images, the presence of carbon nanotubes is clearly observed. A mat of carbon nanotubes covers the surfaces of the LiFePO₄ particles forming LiFePO₄/CNT composite material. The CVD of a carbon gas source generally yields carbon nanotubes having a wide range of carbon nanotube diameters, which is also confirmed by the SEM images.

Figure 2 displays TEM images of the LiFePO₄/CNT composite cathode material. From these HR-TEM images, we observe the presence of carbon nanotubes with thick walls, clear evidence that multiwalled carbon nanotubes have been successfully synthesised. Open cap ends are also observed in Figure 2(a). The dark particles were confirmed by EDS analysis to be that of the LiFePO₄ and also Ni particles, which is to be expected. It is also visible that the carbon nanotubes grow directly from the particles as evident from Figures 2(a) and 2(b). It is thus possible that this technique yields carbon nanotubes grown via the tip growth mechanism.

Figure 3 shows the XRD patterns of the obtained LiFePO₄/CNT composite cathode material. The diffraction peaks were confirmed to be that of olivine LiFePO₄, and no impurities were detected. The XRD pattern could be indexed to the orthorhombic *Pnma* space group (JCPDS card No. 40-1499) based on the well-ordered olivine structure. The intensity of diffraction peaks has a close relation to the crystallinity of the crystal particle. All the XRD peaks are quite sharp and narrow, indicating that highly crystallized LiFePO₄ phase is formed.

Li-ion intercalation/deintercalation reactions essentially depend on electronic conductivity, as the process is accompanied by electron removal at the same time [7]. The carbon nanotubes are added in order to enable the active material (LiFePO₄) to transport lithium ions and electrons at a fast rate. Furthermore, the diffusion of Li ions in the solid state, which is considered to be the slowest process, depends on the surface area [8], which as seen is higher for the LiFePO₄/CNT composites.

To effectively illustrate the effect of carbon nanotube addition on the electron conductivity of the composite materials, electron conductivity measurements were done on the pure LiFePO₄ and the LiFePO₄/CNT composite material. Figure 4 illustrates the electron conductivity results of the material as a function of CNT deposition time (which is directly proportional to CNT content). The increased electrical conductivity with increased CNT deposition time (and, hence, increased CNT content) for the LiFePO₄/CNT cathode material is due to presence of the carbon nanotubes which have higher electrical conductivity. As the CNT content increases, the poorly conductive LiFePO₄ grains are more surrounded by a widening “matrix” of fine, contiguous CNT networks. This is in agreement with the findings of Bewlay et al. [9] and Liu et al. [10] who increased the electrochemical conductivity of LiFePO₄ by the inclusion of carbon or CNT, respectively; however, our materials displayed better charge discharge capacities.

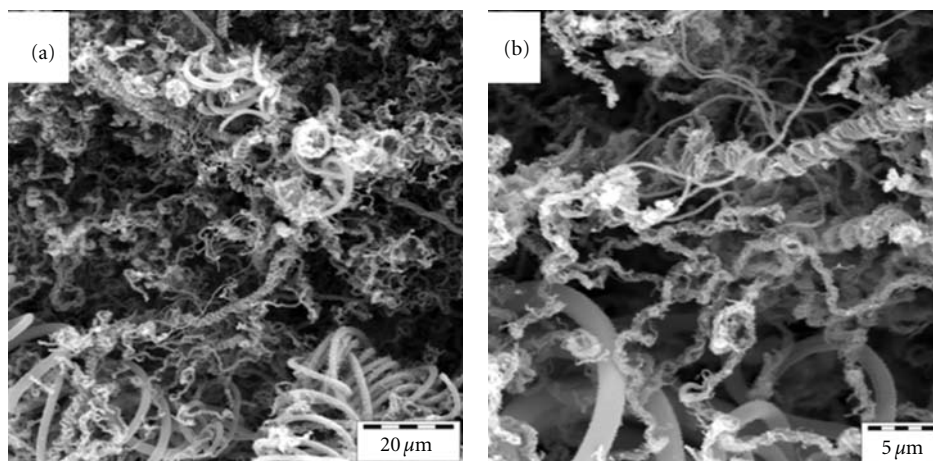


FIGURE 1: SEM images of LiFePO₄/CNT composites synthesised with (a) Ni mist, 60 min deposition at 1000x and (b) Ni mist, 60 min deposition at 3000x magnification.

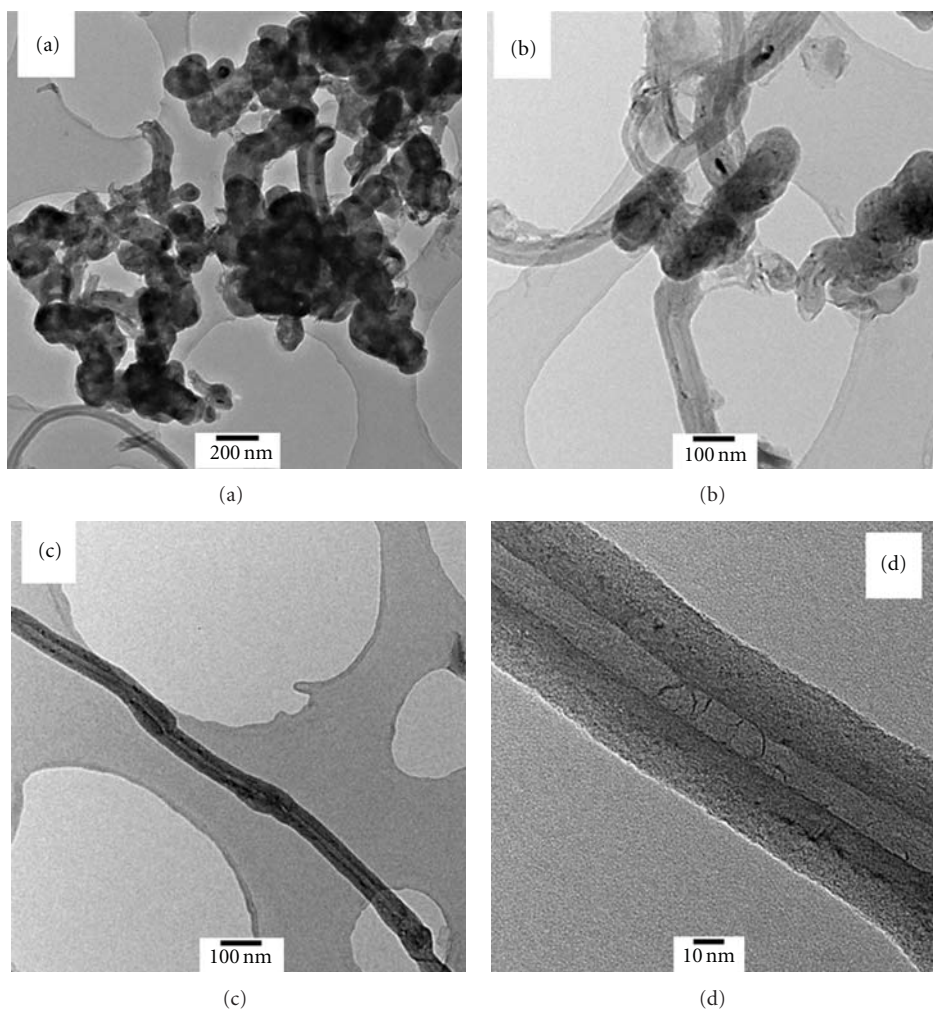


FIGURE 2: HR-TEM images of LiFePO₄/CNT synthesised using the spray pyrolysis-modified CVD technique at (a) 9000x magnification, (b) 17000x magnification, (c) 17000x magnification, and (d) 130000x magnification.

TABLE 2: Surface area and porosity data for the composite $\text{LiFePO}_4/\text{CNT}$ cathode material.

| Material | Single-point BET surface area (m^2/g) | External surface area (m^2/g) | Internal pore area (m^2/g) | Pore volume (cm^3/g) | Average Pore diameter (nm) |
|--|---|---|--|--|----------------------------|
| $\text{LiFePO}_4/\text{CNT}$ Ni mist 60 min dep. | 7.89 | 24.85 | 29.09 | 0.106 | 15.772 |

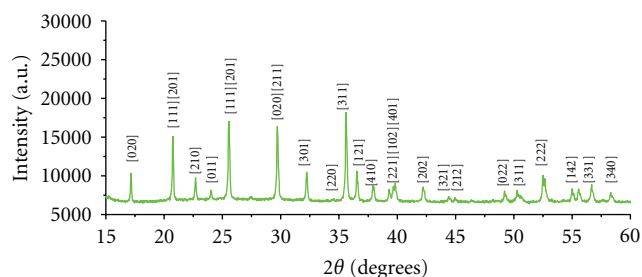
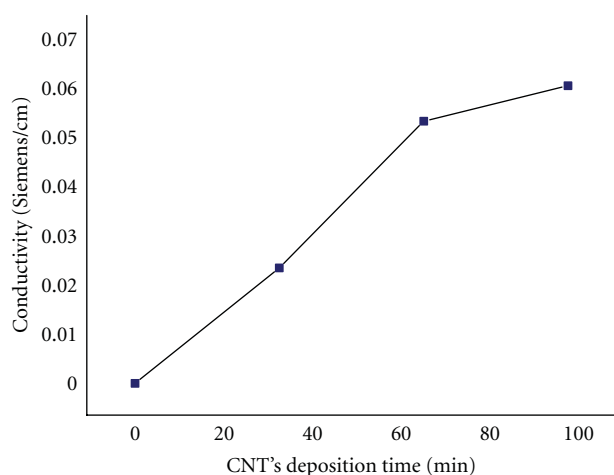
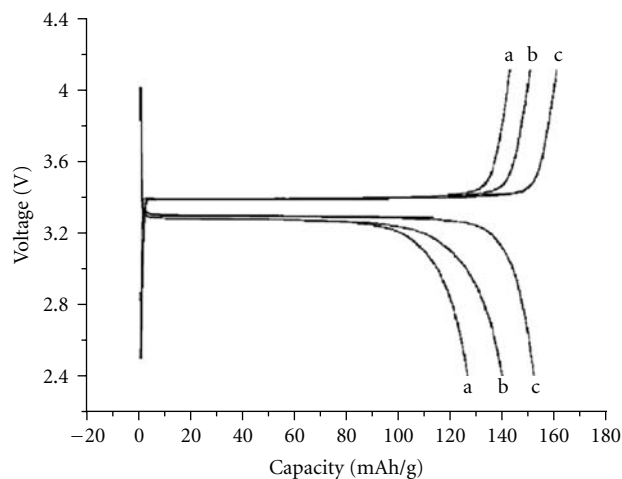
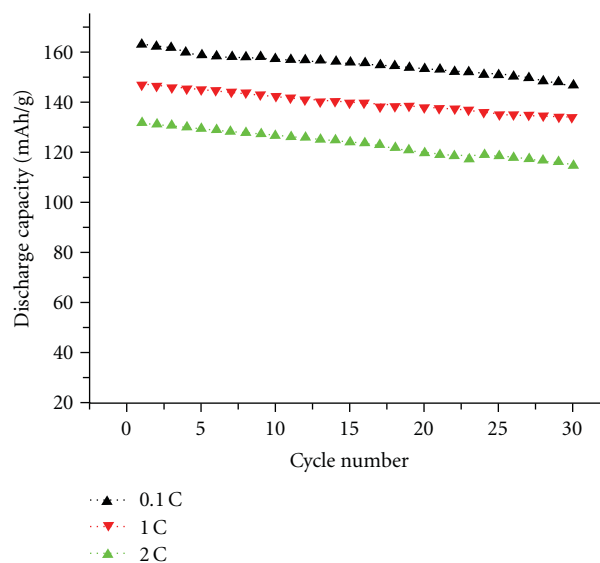
FIGURE 3: XRD patterns of $\text{LiFePO}_4/\text{CNT}$ composite cathode material. The surface area and porosity results obtained for the composite cathode materials are tabulated in Table 2.FIGURE 4: Room temperature conductivity of $\text{LiFePO}_4/\text{CNT}$ as a function of CNT deposition time.

Figure 5 shows the charge/discharge curves at discharge/charge rates varied from 0.1 to 2 C of the $\text{LiFePO}_4/\text{CNT}$ composite material synthesised using the spray-modified CVD technique. In the potential range of 2.5–4.2 V, the composite cathode delivered 163 mAh/g with 94% cycle efficiency at 0.1 C rate in the first cycle. The cycling characteristics of the $\text{LiFePO}_4/\text{CNT}$ cathode material at different discharge rates are shown in Figure 6. The results showed an almost steady decrease in discharge capacity with cycle number, with a capacity fade of approximately 10% after 30 cycles. The cathode displayed discharge capacity of 163 mAh/g at 0.1 C rate and around 134 mAh/g at 2 C rate.

The optimal deposition time required was established from the subsequent charge-discharge testing of the resulting material. The optimal deposition time was found to be 60 minutes when this Ni spray technique was utilised. In this optimal method of $\text{LiFePO}_4/\text{CNT}$ synthesis, a higher

FIGURE 5: Charge/discharge curves of $\text{LiFePO}_4/\text{CNT}$ electrode, at different rates; (a) 2 C, (b) 1 C, and (c) 0.1 C.FIGURE 6: The discharge capacity versus cycle number plot for the $\text{LiFePO}_4/\text{CNT}$ electrode, at different rates.

surface area material was obtained. Well-crystallized carbon nanotubes can improve cycle efficiency due to the reduction of oxide group production and the increased surface area. The electron transport between the cathode-active materials and the current collector was improved due to the fact that the interface was filled with carbon nanotubes. Therefore, the rate capability of this $\text{LiFePO}_4/\text{CNT}$ composite cathode

material was enhanced effectively by the three-dimensional carbon nanotube network.

4. Conclusions

The composite cathode exhibited excellent electrochemical performances with 163 mAh/g discharge capacity at 0.1 C rate in the first cycle. The results indicate that carbon nanotube addition can enable LiFePO₄ to display a higher discharge capacity at a fast rate with high efficiency. The research is of potential interest to the application of carbon nanotubes as a new conducting additive in cathode preparation and for the development of high-power Li-ion batteries for hybrid electric vehicles.

Acknowledgments

The authors acknowledge the NRF and the DST for funding. They would like to acknowledge Dr. R. Butcher at the iThemba LABS for running the XRD analyses.

References

- [1] J. R. Dahn, T. Zheng, Y. Liu, and J. S. Xue, "Mechanisms for lithium insertion in carbonaceous materials," *Science*, vol. 270, no. 5236, pp. 590–598, 1995.
- [2] M. S. Dresselhaus and G. Dresselhaus, "Intercalation compounds of graphite," *Advances in Physics*, vol. 30, no. 2, pp. 139–326, 1981.
- [3] W. Ojczyk, J. Marzec, K. Świerczek et al., "Studies of selected synthesis procedures of the conducting LiFePO₄-based composite cathode materials for Li-ion batteries," *Journal of Power Sources*, vol. 173, no. 2, pp. 700–706, 2007.
- [4] G. Meligrana, C. Gerbaldi, A. Tuel, S. Bodoardo, and N. Penazzi, "Hydrothermal synthesis of high surface LiFePO₄ powders as cathode for Li-ion cells," *Journal of Power Sources*, vol. 160, no. 1, pp. 516–522, 2006.
- [5] X. Z. Liao, Z. F. Ma, L. Wang, X. M. Zhang, Y. Jiang, and Y. S. He, "A novel synthesis route for LiFePO₄/C cathode materials for lithium-ion batteries," *Electrochemical and Solid-State Letters*, vol. 7, no. 12, pp. A522–A525, 2004.
- [6] J. K. Kim, J. W. Choi, G. Cheruvally et al., "A modified mechanical activation synthesis for carbon-coated LiFePO₄ cathode in lithium batteries," *Materials Letters*, vol. 61, no. 18, pp. 3822–3825, 2007.
- [7] R. Dominko, M. Gaberscek, J. Drogenik, M. Bele, S. Pejovnik, and J. Jamnik, "The role of carbon black distribution in cathodes for Li ion batteries," *Journal of Power Sources*, vol. 119–121, pp. 770–773, 2003.
- [8] X. Li, F. Kang, and W. Shen, "A comparative investigation on multiwalled carbon nanotubes and carbon black as conducting additive in LiNi_{0.7}Co_{0.3}O₂," *Electrochemical and Solid-State Letters*, vol. 9, no. 3, pp. A126–A129, 2006.
- [9] S. L. Bewlay, K. Konstantinov, G. X. Wang, S. X. Dou, and H. K. Liu, "Conductivity improvements to spray-produced LiFePO₄ by addition of a carbon source," *Materials Letters*, vol. 58, no. 11, pp. 1788–1791, 2004.
- [10] Y. Liu, X. Li, H. Guo et al., "Effect of carbon nanotube on the electrochemical performance of C-LiFePO₄/graphite battery," *Journal of Power Sources*, vol. 184, no. 2, pp. 522–526, 2008.

Research Article

A New Class of P(VdF-HFP)-CeO₂-LiClO₄-Based Composite Microporous Membrane Electrolytes for Li-Ion Batteries

G. Vijayakumar,¹ S. N. Karthick,² and A. Subramania³

¹ Department of Chemistry, Park college of technology, Anna University, Karumathampatti, Coimbatore 641 659, India

² School of Electrical Engineering, Pusan National University, Jangjeon, Geumjeong, Busan 609-735, Republic of Korea

³ Centre for Nanoscience and Technology, Pondicherry University, Puducherry 605 014, India

Correspondence should be addressed to G. Vijayakumar, ngvijayakumar@yahoo.co.in

Received 28 November 2010; Accepted 14 April 2011

Academic Editor: Dong Shu

Copyright © 2011 G. Vijayakumar et al. This is an open access article distributed under the Creative Commons Attribution License, which permits unrestricted use, distribution, and reproduction in any medium, provided the original work is properly cited.

Composite microporous membranes based on Poly (vinylidene fluoride-co-hexafluoro propylene) P(VdF-co-HFP)-CeO₂ were prepared by phase inversion and preferential polymer dissolution process. It was then immersed in 1M LiClO₄-EC/DMC (v/v = 1 : 1) electrolyte solution to obtain their corresponding composite microporous membrane electrolytes. For comparison, composite membrane electrolytes were also prepared by conventional phase inversion method. The surface morphology of composite membranes obtained by both methods was examined by FE-SEM analysis, and their thermal behaviour was investigated by DSC analysis. It was observed that the preferential polymer dissolution composite membrane electrolytes (PDCMEs) had better properties, such as higher porosity, electrolyte uptake (216 wt%), ionic conductivity (3.84 mS·cm⁻¹) and good electrochemical stability (4.9V), than the phase inversion composite membrane electrolytes (PICMEs). As a result, a cell fabricated with PDCME in between mesocarbon microbead (MCMB) anode and LiCoO₂ cathode had better cycling performance than a cell fabricated with PICME.

1. Introduction

High energy density rechargeable lithium batteries are important to the development of several applications such as portable electronic devices; electric or hybrid cars still requires the optimization of some critical operational features with special concern directed toward those related to safety and design flexibility [1]. Conventional lithium batteries, liquid electrolyte make batteries unsafe due to electrolyte leakage and electrochemical instability due to the repeated oxidation/restoration reaction at the interface between the electrode and electrolyte [2]. To overcome this, polymer electrolytes were introduced that plays an essential role in rechargeable lithium ion batteries. Hence, the control of the miscibility and stability between the liquid electrolytes and the host polymer itself has become one of the prominent factors for polymer electrolytes [3]. Indeed, microporous structure of the host polymer matrix is one of the convenient tools for ionic transport and enhances ionic

conduction [4]. In this regards, P(VdF-co-HFP) host have attracting properties such as high dielectric constant ($\epsilon = 8.4$) and strong electron-withdrawing functional group (-C-F) which may be swollen in carbonate, but does not solvate, therefore facilitates higher concentration of charge carriers. It comprises both an amorphous and crystalline phase where an amorphous phase of the polymer support higher ionic conduction and crystalline phase assists to enhance the mechanical strength for the polymer electrolytes [5]. P(VdF-co-HFP) based polymer electrolyte is one of the most commonly commercialized plastic lithium ion batteries (PLiON) by Telcordia Technologies (formerly Bellcore) since Gozdz et al found the preparation process of porous membrane [6-9]. However, in the process di-butyl phthalate (DBP) extraction step is inconvenient since it increases the cost of the preparation. Some researchers and also our research groups have reported an alternative method to form the porous structure by the phase inversion technique as well as polymer dissolution techniques on the polymer matrix, such

as polyacrylonitrile (PAN) [10, 11], poly(vinylidene fluoride) (PVDF) [12, 13], poly(acrylonitrile-methyl methacrylate) (PAN-MMA) [14, 15] and poly(vinylidene fluoride-co-hexa fluoropropylene) P(VdF-co-HFP) [16–21], and so forth. Moreover, effect of inorganic oxides such as ZrO₂ nanofiller [22], SiO₂ [23, 24], MgO [25], Al₂O₃ [26] and TiO₂ [27–29] on the electrochemical properties of P(VdF-co-HFP) based porous structure polymer electrolytes have been studied. Recently, Rajendran et al. [30] reported a solid polymer electrolyte, with the addition of microscale CeO₂ filler in PMMA polymer matrix. Uvarov et al. has studied the effect of adding some rare earth oxide ceramics such as CeO₂, SiO₂, fly ash, and Eu₂O₃ as dispersoids, and verified the fact that other than γ -Al₂O₃, the above mentioned dispersoids also help in achieving the modest enhancement in electrochemical properties include the ionic conductivity and bulk properties of the composite solid electrolytes [31]. But it is an ever first time we have compared the addition of nanoscale CeO₂ for enhancing the properties of P(VdF-co-HFP) polymer electrolytes [32] by phase inversion and polymer dissolution (removal of PVP additive on the host polymer matrix) techniques which improved the membrane microporous structure world as well as electrochemical behaviour of the composite microporous polymer electrolyte.

In the current research work, we report a new class of P(VdF-co-HFP)-CeO₂ and P(VdF-co-HFP)-CeO₂/ PVP (additive extracted) based polymer electrolytes to seek an importance in the structural and electrochemical properties. This composite microporous membrane electrolyte (PICME/PDCME) has expected to retain excellent electrochemical properties such as ionic conductivity, interfacial stability, electrochemical stability window, and also good cell performance. The morphology and thermal properties of both polymer membranes are described herein. Moreover, the effect of CeO₂ fillers on composite polymer electrolyte and determination of its optimal content further gave a guide line for the preparation of PVP-removed PDCME with good morphological structure and electrochemical properties for rechargeable lithium ion polymer batteries.

2. Experimental Details

2.1. Materials and Its Pretreatment. Poly (vinylidene fluoride-co-hexafluoro propylene) (P(VdF-co-HFP), $M_w = 40,000$) as a host polymer matrix, and lithium perchlorate (LiClO₄) as the electrolyte salt were purchased from Aldrich (USA). The host polymer was dried at 80°C in a vacuum oven under pressure 133.322×10^{-3} Pa (10^{-3} Torr) for 8 h. Nanoscale cerium oxide (CeO₂, average size of ~10–20 nm and surface area ~80–100 m²/g) filler purchased from Aldrich (USA) and LiClO₄ salt were used after drying at 100°C under vacuum for 12 h. Polyvinyl pyrrolidone (PVP, $M_w = 58,000$) was used as an additive received from Across Organic Chemicals (Belgium) and treated under vacuum for 8 h at 60°C. N-methyl pyrrolidone (NMP) obtained from E-Merck. Ethylene carbonate (EC) and dimethyl carbonate (DMC) obtained from Aldrich (USA) were used as plasticizer without further purification.

TABLE 1: Residual weight (%) of PVP after the removal of additive PVP in the composite microporous membranes by preferential polymer dissolution method (PDCM).

| wt% of PVP in P(VdF-co-HFP)-CeO ₂ membrane before removal | Residual wt(%) of PVP in the PDCM after the removal |
|--|---|
| 10 | 0.003 |
| 20 | 0.001 |
| 30 | 0.007 |

2.2. Conventional Phase Inversion Composite Microporous Membrane Electrolytes (PICME). Phase inversion composite microporous membrane (PICM) was prepared by dissolving a certain amount of P(VdF-co-HFP) in NMP solvent with constant stirring to form a homogeneous solution. To this different wt% of CeO₂ (2–10 wt%) filler was added to the polymer solution and stirred continuously for 24 h. The resultant homogenous viscous slurry was cast on a newly cleaned glass plate with desired thickness by using doctor blade. This glass plate was then put into large excess of deionized water for 3–5 h to extract solvent and phase inversion occurred. Mean while, CeO₂ nanoparticles stayed in the polymer matrix during the phase inversion process. The resultant PICM was dried under vacuum pressure at 80°C for 6 h. Finally, dimensionally stable and solvent free PICM with thickness ranging from 70–100 μ m were obtained. These PICM were immersed in 1M LiClO₄ containing 1 : 1 (v/v) ratio of EC and DMC for 6 h to obtain their corresponding phase inversion composite membrane electrolytes (PICMEs).

2.3. Preferential Polymer Dissolution Composite Microporous Membrane Electrolytes (PDCME). Preferential polymer dissolution composite microporous membrane (PDCM) was prepared by dissolving a P(VdF-co-HFP) and different weight (%) of PVP (10, 20 and 30 wt%) in NMP with constant stirring to form homogenous solution. Then the optimized concentration of 8 wt% CeO₂ nanoparticles was dispersed into the polymer solution and stirred continuously for 24 h. The resultant homogenous slurry was spread on a newly cleaned glass plate and a desired thickness was made by doctor blade method. It was allowed to stay in air for few minutes at room temperature, followed by immersing the glass plate into deionized water at 40°C for 3–5 h to obtain PDCM with the removal of PVP, then it was peeled off from the substrate easily. The membrane was dried under vacuum pressure at 80°C for 6 h before and after the treatment. Residual wt% of PVP in the dried PDCM was found out by knowing the wt% of PVP before and after treatment [22] of the membrane from the Table 1. Finally, dimensionally stable and solvent free PDCM with thickness ranging from 70–100 μ m were obtained. These PDCM were immersed in 1M LiClO₄ containing 1 : 1 (v/v) ratio of EC and DMC for 6 h to obtain their corresponding preferential polymer dissolution composite membrane electrolytes (PDCMEs).

The surface morphology of PICM/PDCM was examined by means of JEOL-Field emission scanning electron

microscopy (FE-SEM) with an accelerating voltage range of 20 kV.

Thermal property of PICM/PDCM was investigated by Perkin Elmer—differential scanning calorimetry (Model: Pyris DSC-6) instrument. The measurements were carried out with the heating rate of 10°C/min at nitrogen atmosphere. Crystallinity of PICM/PDCM membranes was calculated from the following equation (1),

$$Xc = \left(\frac{\Delta H_m}{\Delta H_m^\Phi} \right) \times 100, \quad (1)$$

where ΔH_m^Φ is the crystalline melting heat of pure α -PVDF (104.7 J/g), ΔH_m is the heat of melting of P(VdF-co-HFP) based PICM/PDCM.

The porosity of these composite microporous membranes (PICM/PDCM) was measured by immersing the membrane into *n*-butanol for 1 h, weighing the membrane before and after absorption of *n*-butanol and then calculated the porosity using the following equation (2),

$$\text{Porosity } (\rho\%) = \frac{(W_a/\rho_a) \times 100}{(W_a/\rho_a + W_p/\rho_p)}, \quad (2)$$

where W_p is the weight of the dry composite membrane, W_a is the weight of *n*-butanol absorbed by the composite membrane, ρ_a is the density of *n*-butanol and ρ_p is the density of the dry composite membrane.

The electrolyte solution uptake of PICM/PDCM was measured as a function of soaking time in 1 M LiClO₄-EC/DMC (v/v = 1 : 1) for 6 h to obtain their corresponding PICME/PDCME. The electrolyte solution uptake by these membranes was calculated using the following equation (3),

$$\text{solution uptake wt}(\%) = \left[100 \times \frac{(W_f - W_o)}{W_o} \right], \quad (3)$$

where W_f and W_o are the weight of the wet and dry composite membranes (PICM/PDCM), respectively.

The electrolyte solution leakage test for these soaked PICM/PDCMs were carried out by placing the composite membrane electrolyte (PICME/PDCME) in between two filter papers and then squeezed by pressing with a 100 g poly (tetrafluoroethylene) sheet. The weight changes of the membranes containing electrolyte solution was measured every 10 min. We have applied the pressure of $\sim 133.322 \times 10^{-2}$ Pa (10^{-2} torr) to find out the electrolyte leakage studies. The electrolyte solution leakage of the PICME/PDCME was calculated using the following equation (4) described elsewhere [33]:

$$\text{solution leakage wt } (\%) = \left[\frac{(W_i - W_f)}{(W_i - W_o)} \right] \times 100, \quad (4)$$

where W_o is the weight of the dry composite membrane, W_i and W_f are the initial and equilibrium weights of the composite membrane after absorbing the liquid electrolyte, respectively.

To measure the ionic conductivity of PDCMEs and PICMEs, they were sandwiched in between two stainless steel nonblocking electrodes and the measurements were made using HIOKI—LCR Hi-TESTER at a wide frequency range of 10 Hz to 100 KHz at different temperatures ranging from 25 to 80°C. The ionic conductivity of both these PICME/PDCME was determined using conductivity equation; $\sigma = t/(A \times R_b)$ Scm⁻¹, where σ is the conductivity, t is the thickness of the membrane electrolyte, R_b and A are the bulk resistance and cross-sectional area of the membrane electrolyte, respectively. The electrochemical experiments were carried out under inert Argon gas atmosphere.

The interfacial stability of the PICME/PDCME was confirmed by fabricating the cell as Li/electrolyte/Li using EG & G—Electrochemical analyzer over a frequency range of 10 Hz ~ 100 kHz, with an amplitude of 10 mV, for different storage time.

The electrochemical stability window of both these electrolytes was determined by running a linear sweep voltammetry. It was performed by using a two-electrode cell in the configuration of Li/electrolyte/SS (Stainless Steel) in the potential range of 2.0 to 5.5 V versus Li/Li⁺ at a scan rate of 1.0 mVs⁻¹.

Finally, coin type lithium ion cells were assembled by sandwiching the PDCME/PICME in between a mesocarbon microbead (MCMB) anode and a LiCoO₂ cathode. The cell was assembled and then sealed under vacuum in a glove box filled with argon. The cell performance of the PDCME/PICME was evaluated galvanostatically using WonA Tech battery cycle life tester and its performance was compared between PDCME and PICME. At C/2 rate, the test was carried out with a constant current density of 0.25 mAcm⁻² and the cut-off voltage of 3.0 V and 4.2 V.

3. Results and Discussion

3.1. Morphology and Thermal Studies. The morphology of PICM and PDCM is shown in Figure 1. The top surface of PICM containing 8 wt% CeO₂ has shown a sponge like structure and its pores are very tiny and exhibits nearly 1 μ m while that on the bottom surface has shown compact structure and exhibit low degree of pores. The asymmetric distribution of pores appeared on both surface of the membrane can be clearly seen from Figures 1(a) and 1(b). The asymmetric structure is caused by different kinetics during the phase inversion between the two surfaces of the composite membrane. Thus, these two surface facing may differ in morphology to some extent [34]. Further, addition of CeO₂ filler (>10 wt%) on the polymer matrix leads to more rough surface by the growth of aggregates and becomes more compact structure [32]. On contrary, removal of 20 wt% PVP from the PDCM exhibits uniform honeycomb like structure with uniform microporous on both top and bottom surface (1 to 5 μ m) and is shown in Figures 1(c) and 1(d). On the other hand, during the preferential polymer dissolution process, a highly ordered pore structure (i.e., honey comb-like structure) was observed due to the removal of PVP additive from the composite matrices. It

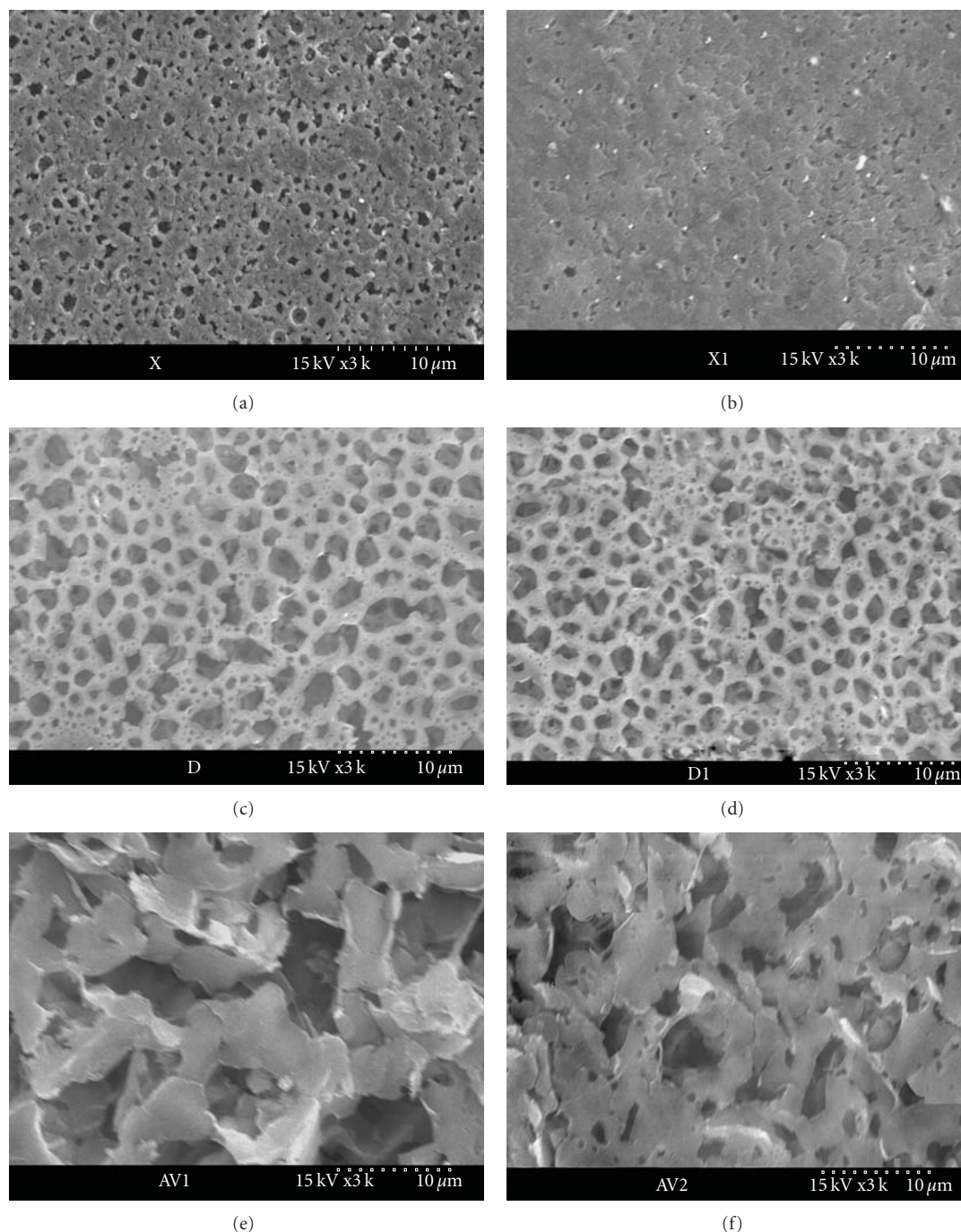


FIGURE 1: FE-SEM images of PICM with the addition of 8 wt% CeO_2 (a) top surface view (b) bottom surface view; PDCM with the removal of 20 wt% PVP from P(VdF-co-HFP)- CeO_2 /removal PVP matrix (c) top surface view (d) bottom surface view; PDCM with the removal of 30 wt% PVP from P(VdF-co-HFP)- CeO_2 /removal PVP matrix (e) top surface view (f) bottom surface view.

could also be an effective track for microporous structure formation on the polymer matrix with high porosity. 30 wt% PVP extracted PDCM showed quite different honey-comb like structure and also large voids were seen on the top and bottom surface (Figures 1(e) and 1(f)). The pore sizes were greater than 5–10 μm and microporous structure become sparser. The residual (negligible) wt% of PVP in the PDCMs was observed after removal of additives (Table 1). It indicates

that negligible wt.% of residual PVP was observed in the PDCMs. It confirms the effective removal of PVP by preferential polymer dissolution process during the treatment of deionized water.

Thermal properties of PICM are illustrated in Table 2. The nanoscale filler incorporation into the polymer matrix decreased the melting temperature ($T_m = 142.2^\circ\text{C}$), and heat of melting ($\Delta H_m = 25.17 \text{ J}\cdot\text{g}^{-1}$) with 8 wt% of

TABLE 2: Thermal and other physical properties of composite microporous membranes obtained by conventional phase inversion method (PICM).

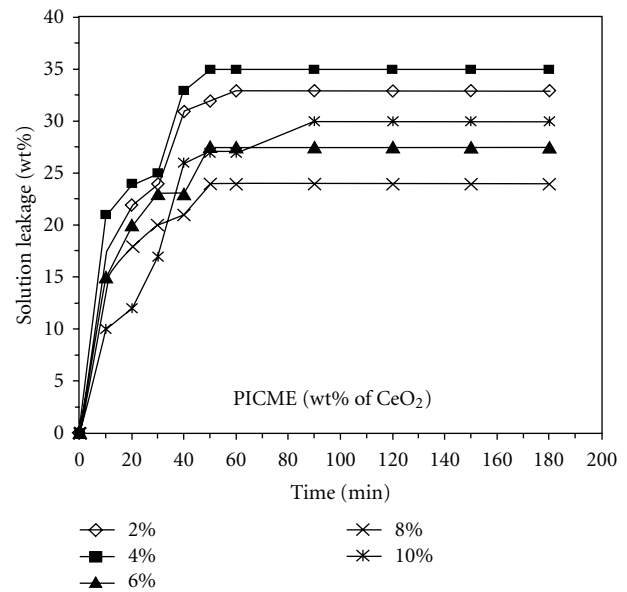
| CeO ₂ (wt%) | PICM | | | | | |
|------------------------|-------|--------------|-----------|------------|--------------------------|---------------|
| | T_m | ΔH_m | X_c (%) | ρ (%) | Electrolyte uptake (wt%) | Film strength |
| 2 | 143.2 | 30.81 | 29.41 | 58 | 124 | Good |
| 4 | 143.1 | 28.72 | 27.43 | 63 | 132 | Good |
| 6 | 142.7 | 27.33 | 26.10 | 66 | 146 | Good |
| 8 | 142.2 | 25.17 | 24.04 | 72 | 150 | Good |
| 10 | 143.1 | 26.54 | 25.34 | 64 | 132 | Good |

CeO₂ filler content. Beyond this filler content enhanced the T_m (143.1°C) and ΔH_m (26.54 J·g⁻¹) due to filler aggregation on the polymer matrix. PDCM with removal of 20 wt% of PVP declined the melting temperature ($T_m = 142.1^\circ\text{C}$) and heat of melting ($\Delta H_m = 24.58 \text{ J}\cdot\text{g}^{-1}$) and are given in Table 3. Moreover, removal of PVP (10 and 20 wt%) on the PDCMs have no drastic changes in thermal properties.

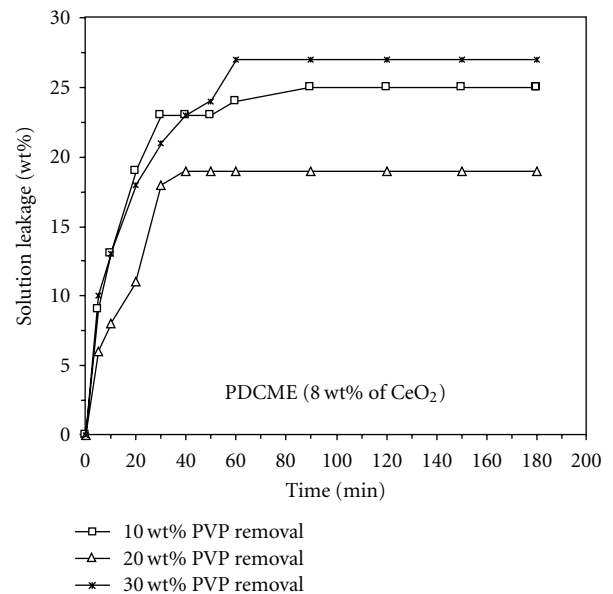
3.2. Porosity, Solution Uptake and Leakage Studies. The porosity values of PICM/PDCMs are given in Tables 2 and 3. It is quite obviously observed that in the case of PICMs, the addition of CeO₂ filler increases the porosity up to 8 wt% CeO₂. Beyond this filler content, porosity was decreased due to aggregation of filler on the polymer matrix [32]. But in the case of PDCMs, the removal of PVP increases the porosity from 79% to 87% continuously. The removal of 20 wt% PVP on the PDCM has the porosity of 85% with good film strength. Beyond this PVP removal, the porosity was higher to 87%, but microporous structure becomes sparser (Figures 1(e) and 1(f)).

Tables 2 and 3, clearly illustrates the electrolyte uptake of both PICM and PDCM even after 6 h. PICM reaches the maximum electrolyte uptake of 150 wt% at optimized CeO₂ (8 wt%) filler concentration (Table 2). But in the case of PDCM reaches maximum electrolyte uptake of 216 wt% with the optimum PVP (20 wt%) extracted membrane (Table 3). Beyond the optimum PVP removal in the PDCM decreased electrolyte uptake owing to the poor pore morphology (Figures 1(c) and 1(d)) and increased the solution leakage (28 wt%). Hence, optimum additive removed PDCME has enhanced liquid electrolyte uptake, due to higher affinity of filler towards the solvents of (EC/DMC) liquid electrolyte solution and also porosity.

The solution leakage of both PICMEs and PDCMEs was studied as a function of time is shown in Figures 2(a) and 2(b). The PICME with 8 wt% of CeO₂ was found to have less solution leakage of 24 wt% after 50min than all other PICME. The PDCME (removal of 20 wt% of PVP) showed very less solution leakage of 19 wt% even after 50min among over all studied membranes. This is due to the modification of rather uniform pores size causes more trapping of liquid electrolyte in the pore walls which helps to avoid solution leakage. But 30 wt% of PVP extracted PDCM has raised solution leakage of 28 wt% after 50min. This is because of macrovoids evident from the morphological studies (Figures



(a)

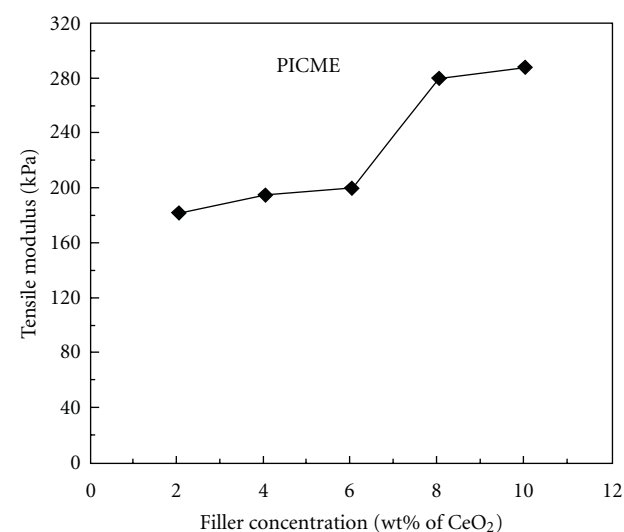


(b)

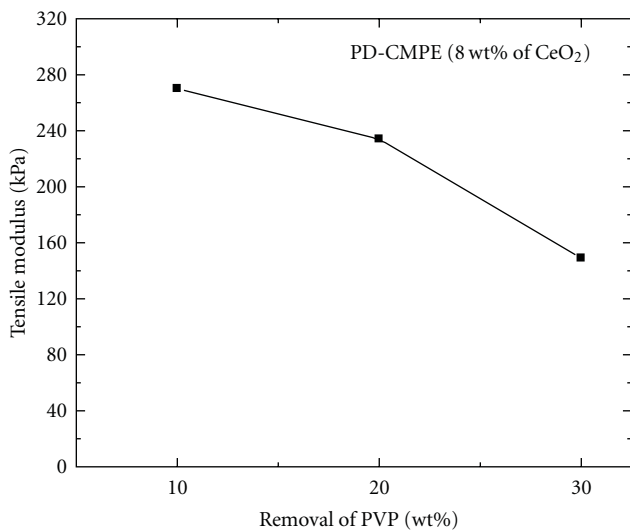
FIGURE 2: Solution leakage versus time of the polymer electrolyte (a) PICMs (b) PDCMs.

TABLE 3: Thermal and other physical properties of composite microporous membranes obtained by preferential polymer dissolution method (PDCMs).

| Removal of PVP (wt%) | T_m | ΔH_m | X_c (%) | PDCM | | |
|----------------------|-------|--------------|-----------|------------|--------------------------|---------------|
| | | | | ρ (%) | Electrolyte uptake (wt%) | Film strength |
| 10 | 142.2 | 24.66 | 23.55 | 79 | 200 | Good |
| 20 | 142.2 | 24.58 | 23.47 | 85 | 216 | Good |
| 30 | 142.0 | 24.07 | 22.98 | 87 | 209 | Moderate |



(a)



(b)

FIGURE 3: Mechanical strength of (a) PICME (b) PDCME.

1(e) and 1(f) which results in fewer amounts of free liquid electrolyte stores in the composite membrane matrix and leads to decrease in ionic conductivity.

3.3. Mechanical Strength. Figure 3(a) shows the tensile strength of PICME as a function of filler content. Mechanical strength of the polymer electrolyte increased with filler

content. The reinforcement mechanism is attributed to the adhesion of inorganic filler to the macromolecular chain [35]. Tensile modulus values of the PICME samples enhanced from 184 kPa to 284 kPa (2 to 8 wt% CeO₂) followed by a small change in tensile modulus values 293 kPa for 10 wt% filler. Figure 3(b) shows the mechanical strength of PDCMEs. It indicates 10 and 20 wt% PVP extracted PDCME has a small loss in mechanical strength related to that of optimized PICME (8 wt% CeO₂), whereas in the case of 30 wt% PVP removed PDCME declined their mechanical strength (149 kPa) due to uneven macrovoids formation and phase separation.

3.4. Electrochemical Studies. The ionic conductivity of PICMEs increased linearly with 2–8 wt% of filler content and attained the maximum ionic conductivity of 2.5 mS·cm⁻¹ (Figure 4(a)). The enhancement of ionic conductivity would be expected due to CeO₂ which interacts with either or both the anion and cation thereby reducing the ion pairing and increases the number of charge carriers [30]. The addition of filler concentration diminish the conductivity, which implies that increased the dilution effect predominate and the conductivity decreases continuously [36]. From the DSC analysis it is found that the crystallinity was reduced due to enhanced polymer segmental motion and also lithium ion migration. Further, the PDCME has enhanced ionic conductivity value of 3.84 mS·cm⁻¹ (Figure 4(b)). It is suggested that PDCME obtained by the removal of 20 wt% of PVP has better performance for Li-ion batteries. In other words, Dey et al. [37] reported increase of amorphous region creates more free volume which enhances the motion of the ionic charge. The increase of conductivity up to 10 wt% ceria is due to Lewis acid-base interaction between filler and PEO. Generally, lithium ion migrates in two route: one route is move along the molecular chain of the polymer and other route is in the amorphous phase of polymer electrolyte [38], where former case is slow transport while the later case is fast. But in the case of PDCME, lithium ion migrates in three routes: one is moving on the microporous gel electrolyte medium, second one is amorphous phase of the polymer electrolyte and third one is filler acts as solid plasticizer to enhance the ion transport. Moreover, uniform microporous structure has enhanced the ionic conductivity.

The Arrhenius plot of Log σ versus 1000/T for the composite membrane electrolytes PICMEs and PDCMEs are shown in Figures 5(a) and 5(b). It is found that the PICME containing 8 wt% CeO₂ has higher ionic conductivity among the systems studied over the whole temperature range of 298–353 K. Moreover, the conductivity increased

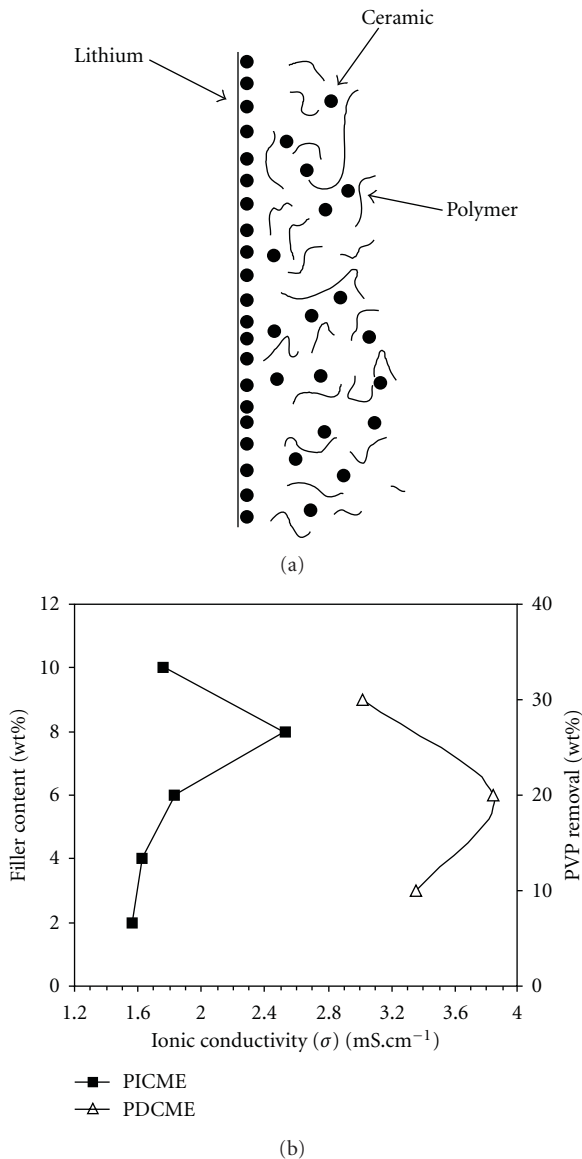


FIGURE 4: (a) The schematic representation of composite polymer electrolyte with the inert filler of nanosized particle (b) Ionic conductivity of (a) PICMEs and (b) PDCMEs at 25°C.

with increase of filler content up to 8 wt% CeO_2 and then decreases with further increase of filler content. In the case of PDCME found that the 20 wt% PVP extracted composite membrane electrolyte containing optimized filler content of 8 wt% CeO_2 has the higher conductivity among the systems studied. But 30 wt% PVP extracted PDCME showed low Log σ value with increase in temperature. It is attributed that the less solution uptake and the electrolyte solution may escape from the composite polymer matrix with increase in temperature. But, PDCME up to 20 wt% PVP extracted membrane was conformed that comparatively less electrolyte solution escape from the composite polymer matrix owing to the uniform microporous morphology.

The interfacial resistance as a function of time is shown in Figures 6(a) and 6(b) and their impedance values

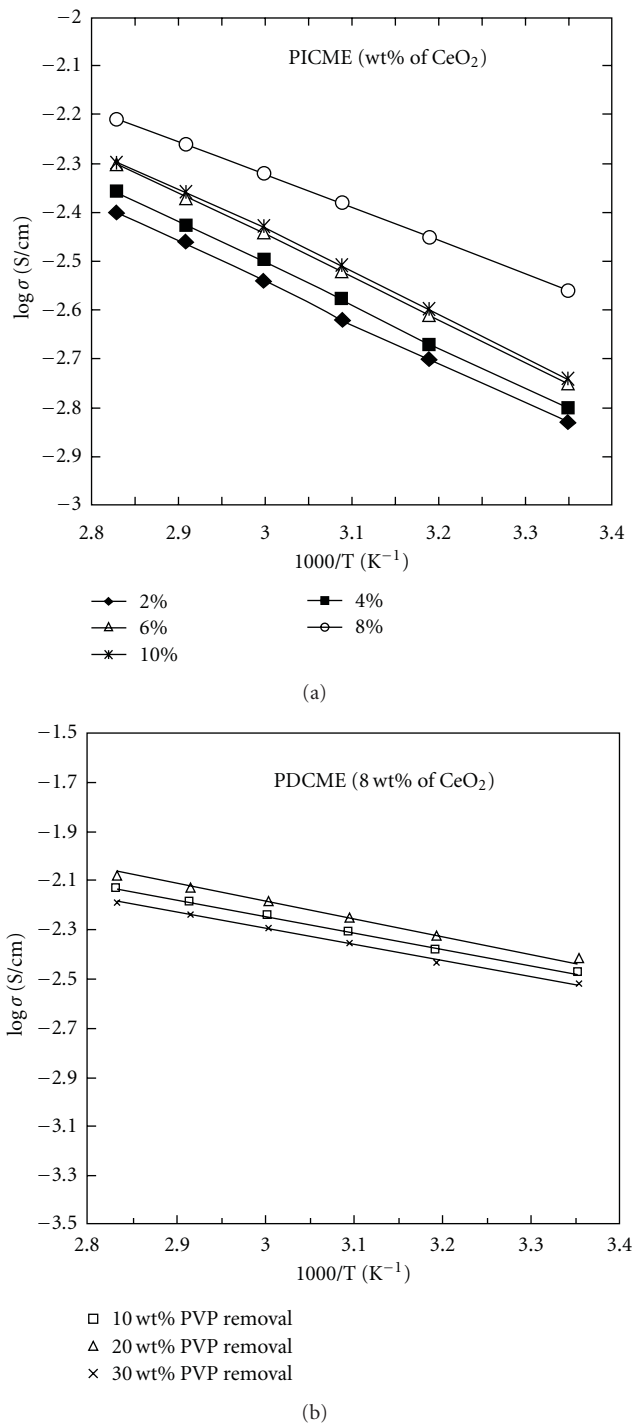


FIGURE 5: Arrhenius plot of (a) PICME with 8 wt% of CeO_2 and (b) PDCME with the removal of different wt% PVP.

were measured from Li/composite microporous membrane electrolyte/Li symmetrical cell kept at room temperature with different storage time. The interfacial resistance was increased gradually and declined with storage time for the PICMEs with 2–8 wt% CeO_2 contents and stabilized after 336 h (2week). It is attributed by assuming that initially slight

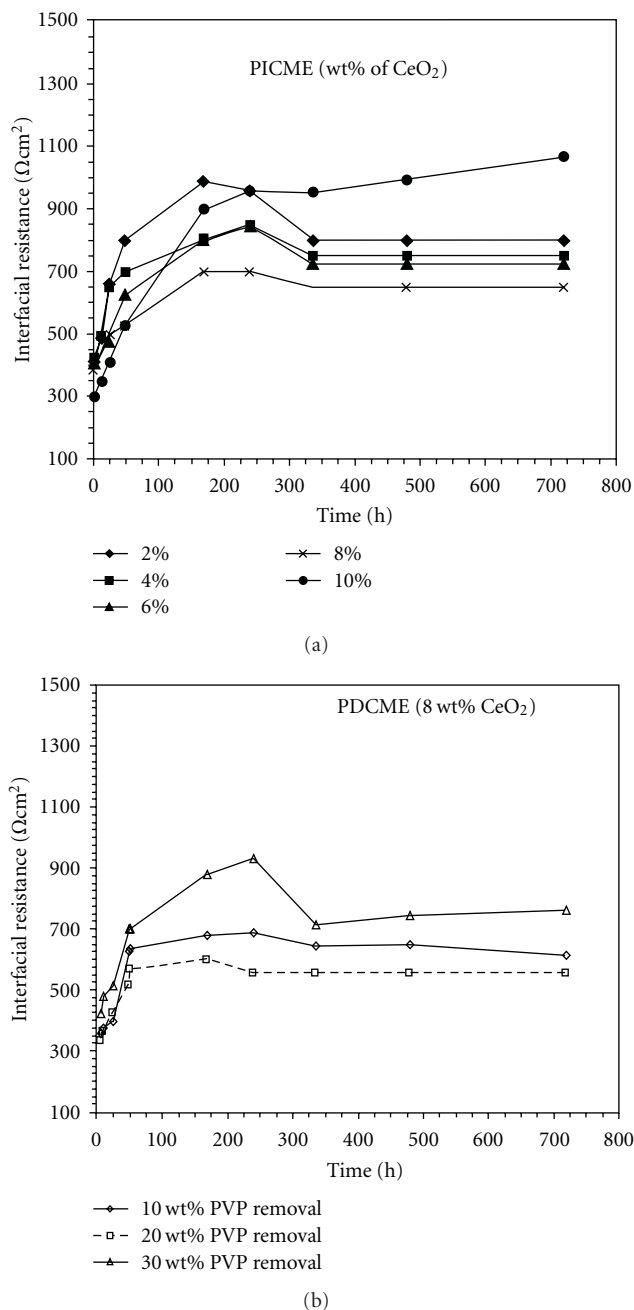


FIGURE 6: Interfacial resistance of the composite microporous membrane electrolyte (a) PICME and (b) PDCME.

passivation layer formed on the lithium metal electrode and the electrolyte solution exhibits more interfacial resistance.

Beyond 8 wt% CeO₂ filler content, the formation of insulating layer (passivation ceramic phase) was increased into the polymer matrix and also impeded the electrode reaction. Generally, the higher interfacial resistance of the polymer electrolytes is based on the growth of passive layer on the lithium electrode surface and the degradation of physical contact between the polymer electrolyte and lithium electrode [12, 39]. At the higher filler content, initial interfacial resistance was declined and sharply increased

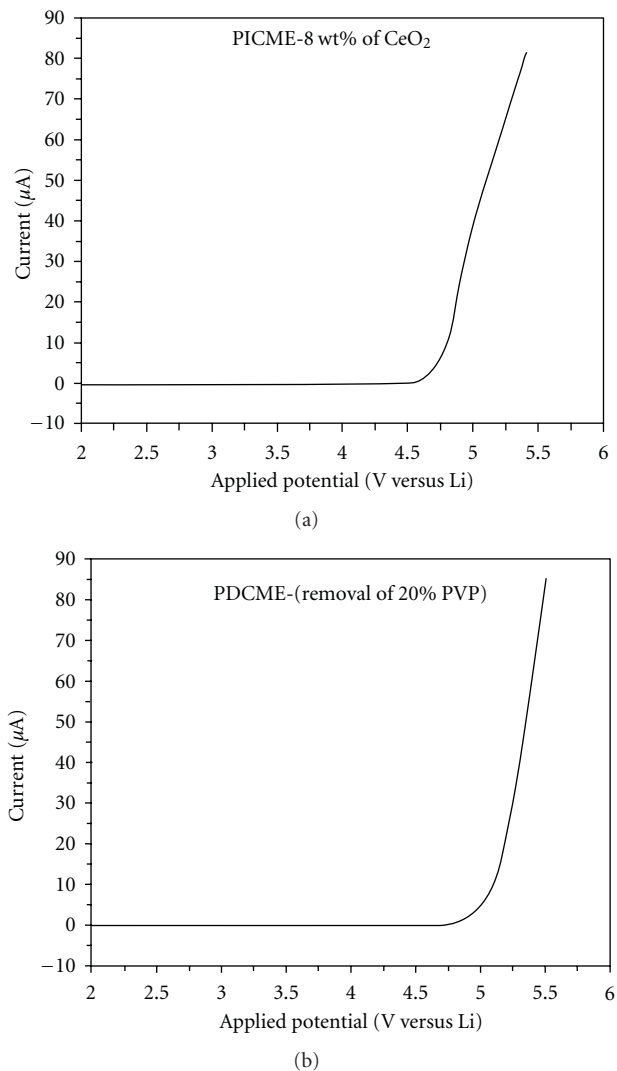


FIGURE 7: Linear sweep voltammetry of the polymer electrolyte (a) PICME and (b) PDCME.

with increasing time. This is due to the formation of thick passivation layer at the electrode surface is feasible at a higher volume fraction of a passive ceramic phase.

Figure 7 displays the current-voltage response by using SS (stainless steel) as a working electrode and lithium metal as a reference electrode measured between the potential ranges of 2.0 to 5.5 V at a scan rate of 1 mVs^{-1} . The onset current flow is associated with the decomposition voltage of the polymer electrolyte. In the decomposition of PDCME no electrochemical oxidation occurs when the voltage is below 4.9 V (versus Li/Li⁺) and the current sharply increases when the voltage is about 5 V (Figure 7(b)). Figure 7(a) shows the decomposition voltage of PICME is about 4.7 V (versus Li/Li⁺). Thus, the oxidation stability of the PDCME is suitable for high-voltage lithium-ion batteries.

A prototype MCMB/composite membrane electrolyte (PICME or PDCME)/LiCoO₂ coin type cell was fabricated to evaluate its cycling performance. LiCoO₂ is widely used

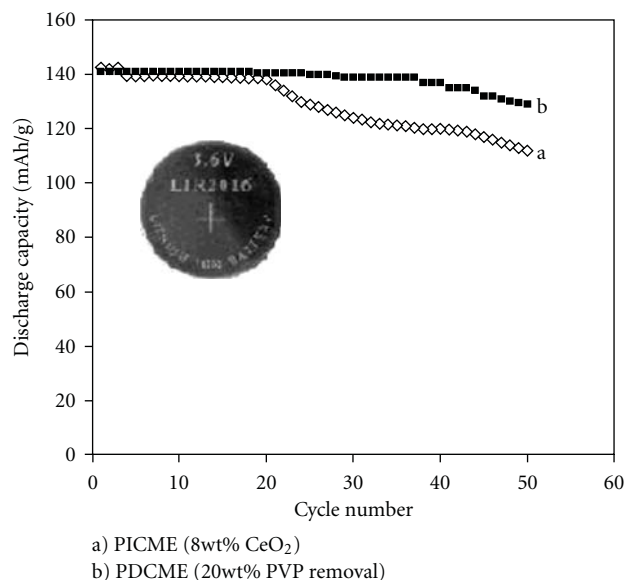


FIGURE 8: Discharge capacity as a function of cycle number for MCMB/electrolyte/LiCoO₂ cells at 25°C with discharge rate of C/2; (a) PICME and (b) PDCME.

as cathode material for conventional lithium ion batteries. The cell was subjected to cycle test with a cut off voltage of 4.2 V for the upper limit and 3.0 V for the lower limit. Figures 8(a) and 8(b) displays the curve of the discharge capacity versus cycle number. The cell with PICME has higher initial discharge capacity 142 mAh/g and declines faster during the cycling test (50th cycle, 18.4% capacity loss) when compared with PDCME (8% capacity loss) at the same cycle. The cell with PDCME delivered a discharge capacity of 141 mAh/g for the initial cycle at C/2 rate. The coulombic efficiency is more than 97% after 10 cycles, and the discharge capacity after 50th cycles is about 92% of its initial discharge capacity. Hence, PDCME showed relatively stable discharge properties, having little capacity fade under constant current and constant voltage conditions at the C/2 rate.

4. Conclusions

P(VdF-HFP)-CeO₂-based composite microporous membranes (PICM/PDCM) have been obtained by adapting conventional phase inversion (CPI) and preferential polymer dissolution (PD) methods. The higher solution uptake and porosity of preferential polymer dissolution composite membrane (PDCM) was achieved by extracting 20 wt% PVP from the composite matrixes and its corresponding PDCME has higher conductivity of 3.84 mS·cm⁻¹ at room temperature than PICME. These optimized PDCME exhibits stable interfacial resistance and provides better electrochemical stability window of 4.8 V with good cycling performance during the discharge at C/2 rate. These results confirmed that the PDCME is considered as the best candidate for the application of lithium-ion polymer batteries rather than PICME.

Acknowledgment

The authors gratefully acknowledge the University Grants Commission (UGC), New Delhi, for giving the financial support to carry out this work.

References

- [1] A. Blazejczyk, W. Wieczorek, R. Kovarsky et al., "Novel solid polymer electrolytes with single lithium-ion transport," *Journal of the Electrochemical Society*, vol. 151, no. 10, pp. A1762–A1766, 2004.
- [2] N. K. Chung, Y. D. Kwon, and D. Kim, "Thermal, mechanical, and electrochemical properties of poly(vinylidene fluoride)-co-hexafluoropropylene/poly(ethylene glycol) hybrid-type polymer electrolytes," *Journal of Power Sources*, vol. 124, no. 1, pp. 148–154, 2003.
- [3] J. Y. Song, Y. Y. Wang, and C. C. Wan, "Review of gel-type polymer electrolytes for lithium-ion batteries," *Journal of Power Sources*, vol. 77, no. 2, pp. 183–197, 1999.
- [4] J. Y. Song, C. L. Cheng, Y. Y. Wang, and C. C. Wan, "Microstructure of poly(vinylidene fluoride)—based polymer electrolyte and its effect on transport properties," *Journal of the Electrochemical Society*, vol. 149, no. 9, pp. A1230–A1236, 2002.
- [5] W. Pu, X. He, L. Wang, C. Jiang, and C. Wan, "Preparation of PVDF-HFP microporous membrane for Li-ion batteries by phase inversion," *Journal of Membrane Science*, vol. 272, no. 1–2, pp. 11–14, 2006.
- [6] W. Xu, K. S. Siow, Z. Gao, and S. Y. Lee, "Ionic conductivity and electrochemical characterization of novel microporous composite polymer electrolytes," *Journal of the Electrochemical Society*, vol. 146, no. 12, pp. 4410–4418, 1999.
- [7] X. Qiu, W. Li, S. Zhang, H. Liang, and W. Zhu, "The microstructure and character of the PVDF-g-PSSA membrane prepared by solution grafting," *Journal of the Electrochemical Society*, vol. 150, no. 7, pp. A917–A921, 2003.
- [8] H. Huang and S. L. Wunder, "Preparation of microporous PVDF based polymer electrolytes," *Journal of Power Sources*, vol. 97–98, pp. 649–653, 2001.
- [9] A. S. Gozdz, C. N. Schmutz, J. M. Tarascon, and P. C. Warren, "Lithium secondary battery extraction method," US Patent no. 5540741, 1996.
- [10] H. S. Min, J. M. Ko, and D. W. Kim, "Preparation and characterization of porous polyacrylonitrile membranes for lithium-ion polymer batteries," *Journal of Power Sources*, vol. 119–121, pp. 469–472, 2003.
- [11] A. Subramania, N. T. Kalyana Sundaram, A. Rohini Priya, R. Gangadharan, and T. Vasudevan, "Preparation of a microporous gel polymer electrolyte with a novel preferential polymer dissolution process for Li-ion batteries," *Journal of Applied Polymer Science*, vol. 98, no. 5, pp. 1891–1896, 2005.
- [12] J. R. Kim, S. W. Choi, S. M. Jo, W. S. Lee, and B. C. Kim, "Electrospun PVdF-based fibrous polymer electrolytes for lithium ion polymer batteries," *Electrochimica Acta*, vol. 50, no. 1, pp. 69–75, 2004.
- [13] Y. Lee Min, J. W. Kim, N. S. Choi, J. Lee An, W. H. Seol, and J. K. Park, "Novel porous separator based on PVdF and PE non-woven matrix for rechargeable lithium batteries," *Journal of Power Sources*, vol. 139, no. 1–2, pp. 235–241, 2005.
- [14] S. S. Zhang, M. H. Ervin, K. Xu, and T. R. Jow, "Li-ion battery with poly(acrylonitrile-methyl methacrylate)-based

- microporous gel electrolyte," *Solid State Ionics*, vol. 176, no. 1-2, pp. 41–46, 2005.
- [15] W. Pu, X. He, L. Wang, Z. Tian, C. Jiang, and C. Wan, "Preparation of P(AN-MMA) microporous membrane for Li-ion batteries by phase inversion," *Journal of Membrane Science*, vol. 280, no. 1-2, pp. 6–9, 2006.
- [16] H. Wang, H. Huang, and S. L. Wunder, "Novel microporous poly(vinylidene fluoride) blend electrolytes for lithium-ion batteries," *Journal of the Electrochemical Society*, vol. 147, no. 8, pp. 2853–2861, 2000.
- [17] J. Y. Song, Y. Y. Wang, and C. C. Wan, "Conductivity study of porous plasticized polymer electrolytes based on poly(vinylidene fluoride) a comparison with polypropylene separators," *Journal of the Electrochemical Society*, vol. 147, no. 9, pp. 3219–3225, 2000.
- [18] D. W. Kim and Y. K. Sun, "Electrochemical characterization of gel polymer electrolytes prepared with porous membranes," *Journal of Power Sources*, vol. 102, no. 1-2, pp. 41–45, 2001.
- [19] Y. Saito, A. M. Stephan, and H. Kataoka, "Ionic conduction mechanisms of lithium gel polymer electrolytes investigated by the conductivity and diffusion coefficient," *Solid State Ionics*, vol. 160, no. 1-2, pp. 149–153, 2003.
- [20] A. Subramania, N. T. K. Sundaram, and G. V. Kumar, "Structural and electrochemical properties of micro-porous polymer blend electrolytes based on PVdF-co-HFP-PAN for Li-ion battery applications," *Journal of Power Sources*, vol. 153, no. 1, pp. 177–182, 2006.
- [21] A. Subramania, N. T. Kalyana Sundaram, and N. Sukumar, "Development of PVA based micro-porous polymer electrolyte by a novel preferential polymer dissolution process," *Journal of Power Sources*, vol. 141, no. 1, pp. 188–192, 2005.
- [22] A. Subramania, N. T. Kalyana Sundaram, A. R. Sathiya Priya, and G. Vijaya Kumar, "Preparation of a novel composite micro-porous polymer electrolyte membrane for high performance Li-ion battery," *Journal of Membrane Science*, vol. 294, no. 1-2, pp. 8–15, 2007.
- [23] A. Du Pasquier, P. C. Warren, D. Culver, A. S. Gozdz, G. G. Amatucci, and J. M. Tarascon, "Plastic PVDF-HFP electrolyte laminates prepared by a phase-inversion process," *Solid State Ionics*, vol. 135, no. 1–4, pp. 249–257, 2000.
- [24] H. Huang and S. L. Wunder, "Ionic conductivity of micro-porous PVDF-co-HFP/PS polymer blends," *Journal of the Electrochemical Society*, vol. 148, no. 3, pp. A279–A283, 2001.
- [25] P. P. Prosini, P. Villano, and M. Carewska, "A novel intrinsically porous separator for self-standing lithium-ion batteries," *Electrochimica Acta*, vol. 48, no. 3, pp. 227–233, 2002.
- [26] Z. Li, G. Su, X. Wang, and D. Gao, "Micro-porous P(VDF-co-HFP) based polymer electrolyte filled with Al₂O₃ nanoparticles," *Solid State Ionics*, vol. 176, no. 23-24, pp. 1903–1908, 2005.
- [27] K. M. Kim, N. G. Park, K. S. Ryu, and S. H. Chang, "Characterization of poly(vinylidene fluoride-co-hexafluoropropylene)-based polymer electrolyte filled with TiO₂ nanoparticles," *Polymer*, vol. 43, no. 14, pp. 3951–3957, 2002.
- [28] K. M. Kim, J. M. Ko, N. G. Park, K. S. Ryu, and S. H. Chang, "Characterization of poly(vinylidene fluoride-co-hexafluoropropylene)-based polymer electrolyte filled with rutile TiO₂ nanoparticles," *Solid State Ionics*, vol. 161, no. 1-2, pp. 121–131, 2003.
- [29] J. D. Jeon, M. J. Kim, and S. Y. Kwak, "Effects of addition of TiO₂ nanoparticles on mechanical properties and ionic conductivity of solvent-free polymer electrolytes based on porous P(VdF-co-HFP)/P(EO-EC) membranes," *Journal of Power Sources*, vol. 162, no. 2, pp. 1304–1311, 2006.
- [30] S. Rajendran, O. Mahendran, and R. Kannan, "Ionic conductivity studies in composite solid polymer electrolytes based on methylmethacrylate," *Journal of Physics and Chemistry of Solids*, vol. 63, no. 2, pp. 303–307, 2002.
- [31] N. F. Uvarov, V. P. Isupov, V. Sharma, and A. K. Shukla, "Effect of morphology and particle size on the ionic conductivities of composite solid electrolytes," *Solid State Ionics*, vol. 51, no. 1-2, pp. 41–52, 1992.
- [32] G. Vijayakumar, S. N. Karthick, A. R. Sathiya Priya, S. Ramalingam, and A. Subramania, "Effect of nanoscale CeO₂ on PVDF-co-HFP-based nanocomposite porous polymer electrolytes for Li-ion batteries," *Journal of Solid State Electrochemistry*, vol. 12, no. 9, pp. 1135–1141, 2008.
- [33] C. G. Wu, M. I. Lu, and H. J. Chuang, "PVdF-co-HFP/P123 hybrid with mesopores: a new matrix for high-conducting, low-leakage porous polymer electrolyte," *Polymer*, vol. 46, no. 16, pp. 5929–5938, 2005.
- [34] M. Mulder, *Basic Principles of Membrane Technology*, Kluwer Academic Publishers, Dordrecht, The Netherlands, 1991.
- [35] R. B. Seymour, *Reinforced Plastics, Properties and Application*, ASM International, Philadelphia, Pa, USA.
- [36] X. Qian, N. Gu, Z. Cheng, X. Yang, E. Wang, and S. Dong, "Impedance study of (PEO)₁₀ LiClO₄-Al₂O₃ composite polymer electrolyte with blocking electrodes," *Electrochimica Acta*, vol. 46, no. 12, pp. 1829–1836, 2001.
- [37] A. Dey, S. Karan, and S. K. De, "Thermal and electric properties of CeO₂ nanoparticles dispersed in polyethylene oxide: NH₄ClO₄ complex," *Solid State Ionics*, vol. 178, no. 39-40, pp. 1963–1968, 2008.
- [38] B. Huang, Z. Wang, L. Chen, R. Xue, and F. Wang, "The mechanism of lithium ion transport in polyacrylonitrile-based polymer electrolytes," *Solid State Ionics*, vol. 91, no. 3-4, pp. 279–284, 1996.
- [39] G. B. Appetecchi, F. Croce, and B. Scrosati, "Kinetics and stability of the lithium electrode in poly(methylmethacrylate)-based gel electrolytes," *Electrochimica Acta*, vol. 40, no. 8, pp. 991–997, 1995.

Research Article

OCV Hysteresis in Li-Ion Batteries including Two-Phase Transition Materials

Michael A. Roscher,¹ Oliver Bohlen,² and Jens Vetter²

¹Institute for Power Electronics and Electrical Drives (ISEA), RWTH Aachen University, 52066 Aachen, Germany

²Division of Energy Storage Systems, BMW AG, 80788 Munich, Germany

Correspondence should be addressed to Michael A. Roscher, michael.roscher@rwth-aachen.de

Received 29 January 2011; Accepted 28 February 2011

Academic Editor: S. Gopukumar

Copyright © 2011 Michael A. Roscher et al. This is an open access article distributed under the Creative Commons Attribution License, which permits unrestricted use, distribution, and reproduction in any medium, provided the original work is properly cited.

The relation between batteries' state of charge (SOC) and open-circuit voltage (OCV) is a specific feature of electrochemical energy storage devices. Especially NiMH batteries are well known to exhibit OCV hysteresis, and also several kinds of lithium-ion batteries show OCV hysteresis, which can be critical for reliable state estimation issues. Electrode potential hysteresis is known to result from thermodynamical entropic effects, mechanical stress, and microscopic distortions within the active electrode materials which perform a two-phase transition during lithium insertion/extraction. Hence, some Li-ion cells including two-phase transition active materials show pronounced hysteresis referring to their open-circuit voltage. This work points out how macroscopic effects, that is, diffusion limitations, superimpose the mentioned microscopic mechanisms and lead to a shrinkage of OCV hysteresis, if cells are loaded with high current rates. To validate the mentioned interaction, Li-ion cells' state of charge is adjusted to 50% with various current rates, beginning from the fully charged and the discharged state, respectively. As a pronounced difference remains between the OCV after charge and discharge adjustment, obviously the hysteresis vanishes as the target SOC is adjusted with very high current rate.

1. Introduction

In the recent years, lithium-ion batteries (Li-ion) became the favorable choice for most portable energy-consuming applications. The demand for high-power capable and high efficient energy storing devices spurred research activities in the field of developing battery electrodes which offer high power and energy densities, comprising long lifetime at minimum cost efforts.

Therefore, new materials, synthesis methods, and improved electrode morphologies are introduced. The electrode material composition and morphology (e.g., grain sizes and distribution) strongly affects the electric characteristics of battery cells. Beyond the utilizable capacity and the power capability, the open-circuit voltage (OCV) is influenced by micromechanic and thermodynamical processes. The OCV hysteresis is a typical phenomenon for batteries and is well documented for nickel-metal-hydride (NiMH) battery systems [1, 2]. Even in Li-ion batteries, OCV hysteresis effects can be observed [2–5], which have a minor impact on battery cells' OCV for cobalt, nickel, or manganese-based cathode

systems, due to the high gradient in the specific state of charge (SOC) to OCV relation. Modern Li-ion cells comprise active materials showing only a slight gradient in the SOC-OCV curves. Herein the OCV hysteresis becomes a major influencing factor for reliable OCV reconstruction, which is a critical task for the model-based state estimation as a part of a battery management system (BMS).

In the following sections, firstly the special OCV characteristics of two-phase transition materials are described with respect to hysteresis phenomena. Then, the electric properties of porous electrode geometries are outlined. Herein a possible explanation for current rate impact on the occurrence of OCV hysteresis is given. Thereafter, validation test results are presented and discussed.

2. Two-Phase Transition Lithium Insertion

Li-ion cells including active materials which perform a two-phase transition during charge and discharge are commonly known to exhibit special OCV characteristic. The lithium iron phosphate (LiFePO_4), lithium titanate ($\text{Li}_4\text{Ti}_5\text{O}_{12}$),

and lithiated graphite (LiC_6) are prominent representatives of active materials performing a two-phase transition lithium insertion and extraction process. Strong interactions between the embedded lithium and the host lattice lead to a phase separation during the two-phase transition [6]. During Li insertion in a delithiated bulk material, a lithiated phase region emerges in juxtaposition to still delithiated phase regions [7, 8]. Further Li insertion leads to a shifting barrier between the phase regions [9, 10]. Analogously, the Li extraction proceeds vice versa. Due to the occurrence of at least two different material phases within, the electrode's electrochemical potential remains almost constant during lithium insertion and extraction, respectively.

That means that, through the occurrence of the two-phase transition a high differential capacity at a certain electrode voltage and therefore a typical voltage plateau during charging or discharging the battery cell can be observed [11]. Figure 1 depicts the typical potential curves (against Li/Li^+) of the aforementioned Li-ion electrode materials, plotted over the stoichiometric lithium content x [12–14].

Both the lithium iron phosphate and lithium titanate comprise one wide potential plateau between lithiated and delithiated states. In contrast, the graphite shows several potential plateaus attributed to all in all five different energetic favorable phase contents. Between the favorable lithiation states, the graphite performs two-phase transitions [12].

Beyond that, cells with two-phase active materials are documented to show pronounced OCV hysteresis [3, 4, 15, 16], where an electrode's potential after Li insertion is lower (against Li/Li^+ reference) than after Li extraction, even with the same stoichiometric Li content. The OCV hysteresis, that is, load history-dependent OCV variation, results from various mechanisms. On one hand, different lattice constants of lithiated and delithiated phases cause mechanical stress at the phase barrier leading to potential drops inside the individual particles [17]. Moreover, lattices distortions, as a result of doping compounds, hinder the propagation of the phase barrier and therefore intensify the mechanical stress in the bulk material [10]. For example, Li-ion battery cathodes consisting of nanosized doped LiFePO_4 are documented to show a difference of approximately 7 mV over a wide range of lithiation between the OCV measured after charge and discharge steps, respectively [15].

Beyond mechanical stress, thermodynamic effects are causing hysteresis in electrode potentials. The energetic favorable lithiation states are related to minima in the free energy of the individual particles of an electrode. The OCV hysteresis is attributed to the varying lithium insertion rates into the particles within a comprehensive electrode. The electrode potentials of a plurality of individual particles yield the resulting electrode potential being different from the progress of the potential of one single particle becoming lithiated. The potential blend of all the particles involved determines the potential of the entire electrode [16].

3. Porous Electrode

The electrodes of Li-ion batteries consist of metal foils (in the majority of cases, copper foil at the anode and aluminum

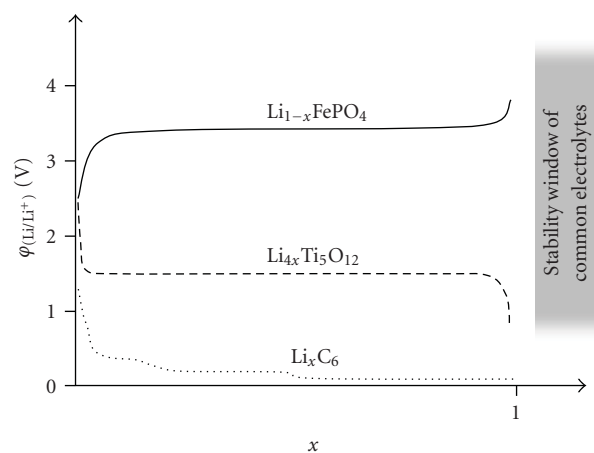


FIGURE 1: Potential against Li/Li^+ of three different electrode materials, showing two-phase transition, plotted over the lithium content x [12–14].

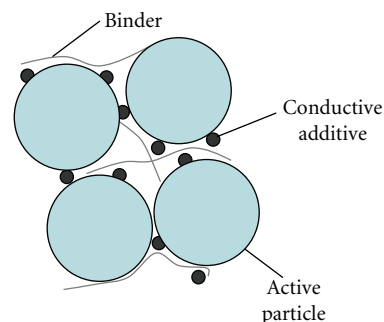


FIGURE 2: Illustration of a small part of an electrode, including active particles, binder, and conductive additives.

foil at the cathode side) coated with a composite including the actual active materials. Beside the active particles, the coating includes binder components (mostly polyvinylidene fluoride) and current conductive additives (e.g., carbon black, carbon nanotubes, etc.). The binder actually causes the mechanical stability of the coating. The conductive additives are mandatory to achieve a good electrical contact among the active particles and between the active material and the metal foils. In Figure 2, the 2D illustration of a small part of the composite electrode material is depicted schematically, where the binder material holds the active materials together, and conductive additives arrange the electric contact from particle to particle.

The electric conductivity of the conductive additives is orders of magnitudes higher than for the most cathode-active materials; especially undoped LiFePO_4 is almost an isolator [18]. Electron conduction within the active material is mainly associated to the lithium insertion/extraction process within the distinct particles. In order to achieve a low ohmic resistance for electron transportation, dopant agents (e.g., W, Mg, Ti, and Al [18]) are added to enhance the active materials' conductivity. Moreover, small-sized active (nano-) particles are incorporated to generate a high surface area and to realize short diffusion lengths inside

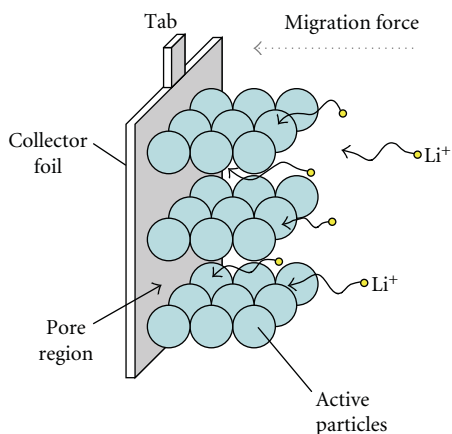


FIGURE 3: Illustration of a porous electrode geometry where lithium ions are inserted.

the active particles. Doping and the usage of small particles reduce electric losses within the active particles. Even the electric conductivity of the actual active material can be increased significantly, and the electron migration between the particles and the collector foils during load mainly occurs within the conductive additives. A high content of additives enables a good electron transport from the current collector towards the active particles and vice versa. However, the electric contact differs from particle to particles. Especially for nanoparticles contacting with additives or coating within conductive carbon layers it is a critical issue [14, 16]. Hence, some particles have a better contact to the collector foil than other particles. Particles with a good electric contact are therefore favorable current paths during charge/discharging of the electrode, also yielding a nonuniform lithium insertion and extraction. Especially, during high current charging and discharging, the voltage drops along the various current paths have major impact on the Li insertion/extraction rate distribution among the active particle of an electrode.

Beside the electronic contact, the ionic contact at the interface between active material and the electrolyte is critical to achieve a good electrode performance. Therefore, small-sized active particles and a high porosity are preferable. High porosity yields a high amount of liquid electrolyte within the electrode and therefore generates a good ionic contact of the active particles. Furthermore, high porosity enables a fast ion exchange between the electrodes of a battery as more ions can migrate within in the wider pores of an electrode. But high porosity is counteracted by a lower energy density and an electronic contacting of the particles. So the optimum porosity, determined by calendaring the coated foils, is a trade-off between the mentioned properties [19].

A simplified illustration of a porous electrode is depicted in Figure 3, where pore regions exist between the active particles (binder and conductive additives are not shown).

During Li insertion, the ions migrate from the counterelectrode towards the active particles where the insertion occurs. During Li insertion, the Li^+ ion concentration within the pores decreases as the ions are absorbed by the active material. To reach the inner particles, the ions propagate

within the pores (migration and diffusion forced) from the electrode surface towards the inner regions. Due to Kohlrausch's law, the ion conductivity of the electrolyte within the pores decreases as the ion concentration decreases [20]. A lower ionic conductivity within the inner pore regions makes the Li insertion in the electrode's outermost particles more favorable, also yielding a nonuniform phase transformation among the particles. At high ion conduction rates, that is, high charge/discharge currents, the ion concentration variation along the pores depth increases, additionally forcing a more nonuniform Li insertion process among the particular particles.

As aforementioned, the hysteresis of two-phase transition materials (i.e., higher electrode potential against Li/Li^+ after Li extraction than after Li insertion, at the same stoichiometric Li content) refers to microscopic effects within the particles and the distributed Li insertion/extraction among the particles. After low current rate SOC adjustment (e.g., to SOC = 50%), the stoichiometric Li content of the particles can be assumed to be normally distributed, due to variations of particle sizes and variation of the electric/ionic contact of the individual particles, and therefore OCV hysteresis can be observed (e.g., in LiFePO_4 electrodes [15, 16]).

Through high-load application, the Li insertion/extraction rates and therefore the Li contents within the particles cannot be assumed to be normally distributed, due to diffusion limitations within the porous electrode. The Li insertion in an electrode's outermost region proceeds significantly faster than the insertion into in the inner regions, as a consequence of ion depletion within the pores. The outermost particles become completely transformed into the lithiated state, and the inner particles remain almost delithiated. The strong Li content variance among the delithiated and lithiated particles yields an equalization ion exchange between the particles after a certain mid-SOC is adjusted. During this subsequent relaxation, the former almost delithiated inner particles become more lithiated, and the electrode's outer particles release Li. The process is equal to a case where almost one-half of the electrode is charged and the other part is discharged. Thus, after relaxation, the potential (against Li/Li^+) of the comprehensive electrode lies between the potential after Li insertion and the potential after Li extraction, respectively. Hence, the remaining hysteresis shrinks as the SOC is adjusted with higher currents, due to the stronger nonuniformity among the particles' Li contents. Measurements to validate the mentioned correlation on Li-ion cells including two-phase transition materials are documented in the following sections.

4. Experimental

Electrical tests on individual cells are done on a Digatron test bench (± 6 V). Tests are carried out on prototype Li-ion cells, including LiFePO_4 -based cathode and graphite-based anode. Both active materials are known to perform a two-phase transition and comprise OCV hysteresis, as well.

To give insight to the OCV hysteresis characteristics of the encountered cells, full-cycle tests are carried out. The cells are fully charged through CCCV (constant current

0.5 C (C-rate), constant voltage 3.6 V for 1 hour) charging regime (\rightarrow SOC = 100%). After 30 minutes rest, the cells are gradually discharged in 5% Δ SOC steps (according to the nominal capacity). Every discharge step a relaxation time of 3 hours (in open-circuit condition) is included. The gradual discharge is repeated until 100% of the nominal capacity is extracted. Then, the cells are gradually charged again (5% Δ SOC steps, 0.5 C current, 3 hours rest, included each step) until the cutoff voltage of 3.6 V is reached.

In order to investigate the impact of the load current rate on the occurrence and extent of the actual hysteresis, the cells' SOC = 50% is adjusted by charging of empty cells (SOC = 0%, in relation to the cells' nominal capacities) and by discharging of completely charged cells (SOC = 100%). The charge/discharge sequences are carried out with two different current rates. First, the target SOC = 50% is adjusted with 0.5 C. Thereafter, the cell individual open-circuit voltages are tracked for 8 hours. This test procedure is repeated with a current rate of 10 C for adjusting an SOC = 50%. Again, the OCV progresses are logged for 8 hours after the SOC adjustment is finished.

During testing, the cells under investigation are placed in a climate chamber from CTS, and the cells' ambient temperatures are constantly held at 25°C.

5. Results and Discussion

Through gradual discharging and subsequent charging of single cells, the relation between SOC and OCV is obtained. A typical progress of the OCV, measured after 3-hour relaxation time, plotted over the distinct SOC values, is illustrated in Figure 4.

Two facts are obvious from the shown results. First, the OCV after the certain discharge steps (marked with $OCV_{\text{discharge}}$) is significantly lower than the OCV after charging (OCV_{charge}). Hence, two curves exist, enclosing a hysteresis. The voltage gap between both curves depends on the SOC, where a maximum gap of approximately 40 mV can be found at SOC = 25%. Second, the OCV curves comprise significant plateaus and edges referring to the edges and plateaus of the graphite anode (see Figure 1). In the illustrated curves, the potential edge related to the stoichiometric state $Li_{0.5}C_6$ lies in the range SOC = 65–75% of the investigated prototype cells. Hence, the increasing gradient towards the fully charged state, is attributed to the potential of the $LiFePO_4$ -based cathode. Near to the fully charged state the hysteresis voltage gap decreases, but it is still apparent in the tested case, after 3 hours of rest. Due to the long rest periods in between each charge/discharge step and from this first test, the OCV hysteresis can be assumed to be stable, at least from the practical point of view.

To give further insight on how the current rate influences the extent of the OCV hysteresis, the second OCV tests is carried out. The progress of the measured cell voltages after the SOC = 50% is adjusted through charging and discharging (with 0.5 C and 10 C, resp.) is depicted in Figure 5.

Obviously, the OCV values after 8-hour relaxation time differ significantly, even if the SOC is exactly the same in all the four given cases. The OCV difference after low-current

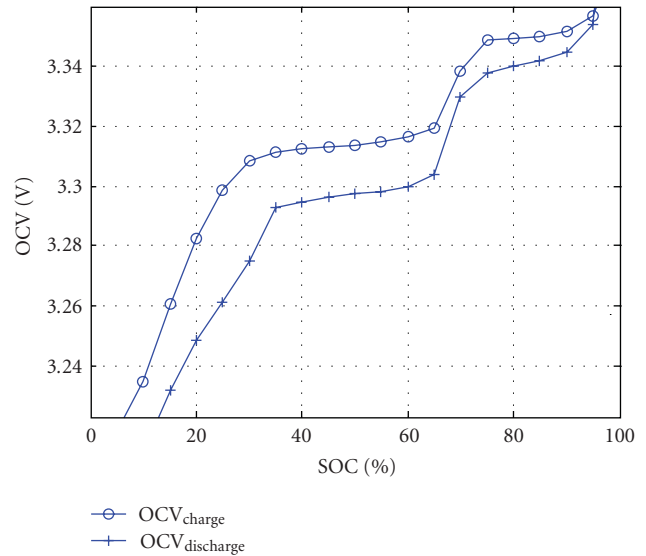


FIGURE 4: OCV after 3 hours rest plotted over the SOC, after stepwise discharging and charging with 0.5 C.

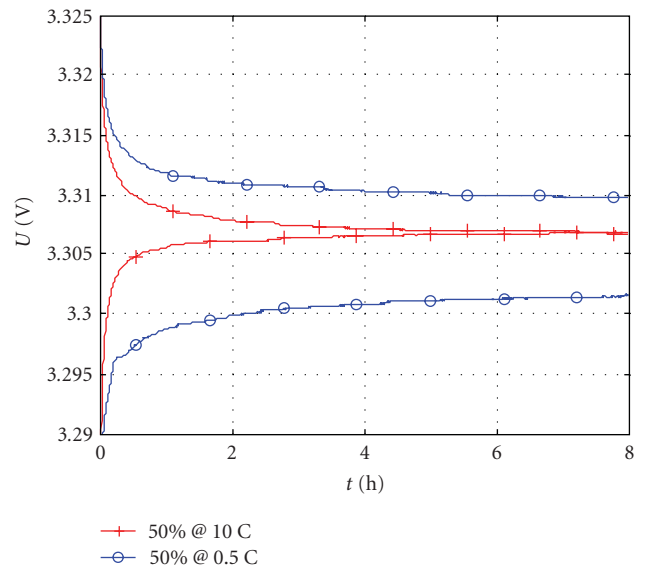


FIGURE 5: Progress of the cell voltage during rest over 8 hour, where the SOC = 50% is adjusted through charging and discharging with various current rates.

load is approximately 8 mV, whereas no difference remains as SOC = 50% is adjusted with 10 C, being independent from the current direction. Noticeably, the OCV hysteresis has completely vanished after high-load application. Herein, the relaxation takes approximately 5 hours until the voltages have completely converged. After shorter rest durations, a slight OCV hysteresis would be observed.

In comparison to the voltage gap between charge and discharge OCV curve at SOC = 50% of approximately 18 mV in Figure 4 (gradual cycle test), the gap after 0.5 C load (one charge/discharge step to SOC = 50%) is only 11 mV. Hence, the higher mean current during SOC adjustment in one

straight step (0.5 C) in comparison to the OCV test with gradual steps (0.5 C with 3 hours of rest every 5% Δ SOC step) already yields a reduced voltage hysteresis.

On one hand, the test results confirm the hypothesis outlined in Section 3. Interparticle charge transfer, resulting from strong inhomogeneities among the particles' lithium contents, is a reasonable explanation for a shrinking OCV hysteresis with increasing current application.

On the other hand, the results show that the relaxation takes several hours (at room temperature) and therefore proceeds very slowly, giving a hint that the occurring processes are attributed to very slow solid-state diffusion processes from particle to particle. Even the voltages after low-current SOC adjustment are drifting for approximately 5 hours until a steady state is reached. Hence, at temperatures below zero degrees, the relaxation is supposed to take even more time than in the presented cases, due to the decreasing diffusion constants at low temperatures. Thus, stepwise OCV measurements at low temperature on Li-ion cell and even half cells should include rest periods of several hours to achieve reliable results. But this aspect has not been completely enlightened yet.

The impact of the current rate on the occurrence of OCV hysteresis and the very slow OCV recovery are critical for commonly used model-based battery state estimation methods. Evaluating battery cells' OCV values is in many cases a reliable way to estimate the SOC—in the shown cases it would not. The presented results point out that for Li-ion cells including two-phase transition active materials, long rest periods are to be considered to evaluate the OCV in order to achieve the instantaneous SOC. Moreover, methods are mandatory to reconstruct the impact of the current rate on the occurrence and extent of the actual hysteresis voltage. For implementation in battery management systems, physical models may be too complex, being not suitable for a fast real-time calculation. Expert systems and artificial neural network (ANN) will be more promising. However, the development of one of the latter-mentioned systems, operating reliably under every operation condition, lies beyond the scope of this work and is therefore left out here.

The results given in this section are based on measurements on a certain type of Li-ion cells including LiFePO_4 -based cathode and graphite anode. For lithium titanate ($\text{Li}_4\text{Ti}_5\text{O}_{12}$), also performing a two-phase transition over a wide SOC range, hysteresis effects are not documented yet. However, Li-ion cells including LiFePO_4 cathodes and $\text{Li}_4\text{Ti}_5\text{O}_{12}$ anodes can even though show pronounced OCV hysteresis, due to the cathode characteristics. Hence, investigations on the OCV hysteresis of the latter-stated cell technology are a topic of our future research.

6. Conclusion

The current intensity during load of Li-ion battery cells, including two-phase transition active materials, influences the Li insertion/extraction rate among the particles of the electrodes. High current rates are assumed to yield strong inhomogeneities in the particles' lithium contents and therefore induce an ion transfer from lithiated particle

towards delithiated particles. The test results show that high current load affects the macroscopic processes in a way that OCV hysteresis vanishes for Li-ion cells, which are regularly showing OCV hysteresis after low current application.

To quantify and reconstruct the illustrated effects under various conditions new methods are to be encountered, considering the load current intensity besides the SOC, the temperature, and the load current direction as factors influencing the OCV hysteresis.

References

- [1] M. Thele, O. Bohlen, D. U. Sauer, and E. Karden, "Development of a voltage-behavior model for NiMH batteries using an impedance-based modeling concept," *Journal of Power Sources*, vol. 175, no. 1, pp. 635–643, 2008.
- [2] K. P. Ta and J. Newman, "Proton intercalation hysteresis in charging and discharging nickel hydroxide electrodes," *Journal of the Electrochemical Society*, vol. 146, no. 8, pp. 2769–2779, 1999.
- [3] J. Barker, R. Pynenburg, R. Koksang, and M. Y. Saidi, "An electrochemical investigation into the lithium insertion properties of Li_xCoO_2 ," *Electrochimica Acta*, vol. 41, no. 15, pp. 2481–2488, 1996.
- [4] A. K. Sleight, J. J. Murray, and W. R. McKinnon, "Memory effects due to phase conversion and hysteresis in $\text{Li}/\text{Li}_x\text{MnO}_2$ cells," *Electrochimica Acta*, vol. 36, no. 9, pp. 1469–1474, 1991.
- [5] D. Carlier, I. Saadoun, M. Ménétrier, and C. Delmas, "Lithium electrochemical deintercalation from $\text{O}_2\text{-LiCoO}_2$: structure and physical properties," *Journal of the Electrochemical Society*, vol. 149, no. 10, pp. A1310–A1320, 2002.
- [6] M. D. Levi and D. Aurbach, "Frumkin intercalation isotherm—a tool for the description of lithium insertion into host materials: a review," *Electrochim Acta*, vol. 45, pp. 167–185, 1999.
- [7] C. V. Ramana, A. Mauger, F. Gendron, C. M. Julien, and K. Zaghib, "Study of the Li-insertion/extraction process in $\text{LiFePO}_4/\text{FePO}_4$," *Journal of Power Sources*, vol. 187, no. 2, pp. 555–564, 2009.
- [8] L. Laffont, C. Delacourt, P. Gibot et al., "Study of the $\text{LiFePO}_4/\text{FePO}_4$ two-phase system by high-resolution electron energy loss spectroscopy," *Chemistry of Materials*, vol. 18, no. 23, pp. 5520–5529, 2006.
- [9] J. Goodenough, A. Padhi, K. S. Nanjundaswamy, and C. Masquelier, "Cathode materials for secondary (rechargeable) lithium batteries," US patent 5910382, 1999.
- [10] N. Meethong, H. Y. S. Huang, S. A. Speakman, W. C. Carter, and Y. M. Chiang, "Strain accommodation during phase transformations in olivine-based cathodes as a materials selection criterion for high-power rechargeable batteries," *Advanced Functional Materials*, vol. 17, no. 7, pp. 1115–1123, 2007.
- [11] M. A. Roscher, J. Vetter, and D. U. Sauer, "Characterisation of charge and discharge behaviour of lithium ion batteries with olivine based cathode active material," *Journal of Power Sources*, vol. 191, no. 2, pp. 582–590, 2009.
- [12] M. Winter, J. O. Besenhard, M. E. Spahr, and P. Novák, "Insertion electrode materials for rechargeable lithium batteries," *Advanced Materials*, vol. 10, no. 10, pp. 725–763, 1998.
- [13] N. Meethong, H.-Y. Shadow Huang, C. Crater, and Y.-M. Chiang, "Size-dependent lithium miscibility gap in nanoscale $\text{Li}_{1-x}\text{FePO}_4$," *Electrochemical and Solid-State Letters*, vol. 10, pp. A134–A138, 2007.

- [14] G. J. Wang, J. Gao, L. J. Fu, N. H. Zhao, Y. P. Wu, and T. Takamura, "Preparation and characteristic of carbon-coated $\text{Li}_4\text{Ti}_5\text{O}_{12}$ anode material," *Journal of Power Sources*, vol. 174, no. 2, pp. 1109–1112, 2007.
- [15] N. Meethong, Y.-H. Kao, S. Speakman, and Y.-M. Chiang, "Structural and electrochemical studies of aliovalent cation doped olivines," in *Proceedings of the Pacific Rim Meeting on Electrochemical and Solid-State Science*, Honolulu, Hawaii, USA, 2008.
- [16] W. Dreyer, J. Jamnik, C. Gohlke, R. Huth, J. Moškon, and M. Gaberšček, "The thermodynamic origin of hysteresis in insertion batteries," *Nature Materials*, vol. 9, no. 5, pp. 448–453, 2010.
- [17] U. S. Kasavajjula, C. Wang, and P. E. Arce, "Discharge model for LiFePO_4 accounting for the solid solution range," *Journal of the Electrochemical Society*, vol. 155, no. 11, pp. A866–A874, 2008.
- [18] M. Thackeray, "Lithium-ion batteries: an unexpected conductor," *Nature Materials*, vol. 1, no. 2, pp. 81–82, 2002.
- [19] C. Fongy, A. C. Gaillot, S. Jouanneau, D. Guyomard, and B. Lestriez, "Ionic vs electronic power limitations and analysis of the fraction of wired grains in LiFePO_4 composite electrodes," *Journal of the Electrochemical Society*, vol. 157, no. 7, pp. A885–A891, 2010.
- [20] F. W. G. Kohlrausch, *Das Leitvermögen der Elektrolyte, Insbesondere der Lösungen*, Taschenbuch, BiblioBazaar, Charleston, SC, USA, 2009.

Research Article

Influence of the C/Sn Ratio on the Synthesis and Lithium Electrochemical Insertion of Tin-Supported Graphite Materials Used as Anodes for Li-Ion Batteries

Cédric Mercier,¹ Raphaël Schneider,² Patrick Willmann,³ and Denis Billaud¹

¹Laboratoire de Chimie du Solide Minéral, Nancy-University, CNRS, BP 239,
54506 Vandoeuvre-les-Nancy Cedex, France

²Laboratoire Réactions et Génie des Procédés (LRGP), UPR 3349, Nancy-University, CNRS, 1 rue Grandville,
54001 Nancy Cedex, France

³Centre National d'Etudes Spatiales (CNES), 18 Avenue E. Belin, 31055 Toulouse Cedex, France

Correspondence should be addressed to Denis Billaud, denis.billaud@lcsm.uhp-nancy.fr

Received 21 January 2011; Accepted 25 February 2011

Academic Editor: S. Gopukumar

Copyright © 2011 Cédric Mercier et al. This is an open access article distributed under the Creative Commons Attribution License, which permits unrestricted use, distribution, and reproduction in any medium, provided the original work is properly cited.

Novel composites consisting of tin particles associated to graphite were prepared by chemical reduction of tin(+2) chloride by *t*-BuONa-activated sodium hydride in the presence of graphite. The samples obtained using various C/Sn ratios were investigated by X-ray powder diffraction (XRD), transmission electron microscopy (TEM), scanning electron microscopy (SEM), and elemental analyses. The largest tin particles associated to graphite layers were observed for the material with a C/Sn ratio of 16. For the materials with C/Sn ratios of 42 and 24, SEM and TEM experiments demonstrated that Sn aggregates of ca. 250 nm length and composed of Sn particles with an average diameter of ca. 50 nm were homogeneously distributed at the surface of graphite. Electrodes prepared from the C/Sn = 42 material exhibit a high reversible capacity of over 470 mAhg⁻¹ up to twenty cycles with stable cyclic performances.

1. Introduction

With the development of portable electronic devices and the enormous interest in the hybrid electric vehicle market, the demand for power sources with higher storage capacity, longer operating times, as well as safety, environmental compatibility, and low production costs has markedly increased [1].

Graphite is mainly used as negative electrode materials for lithium ion secondary batteries and yields a theoretical capacity of 372 mAhg⁻¹. Lithium alloys, which can be reversibly formed and decomposed electrochemically in nonaqueous electrolyte solutions, are natural alternative candidates to both lithium and lithiated graphite in rechargeable Li-based batteries. Of special importance in this respect are the lithium-tin compounds. Indeed, both metallic tin and tin oxide (SnO₂) were shown as interesting anode materials for Li-ion batteries because of their conducting properties combined with high specific capacities (Sn, 994 mAhg⁻¹ and

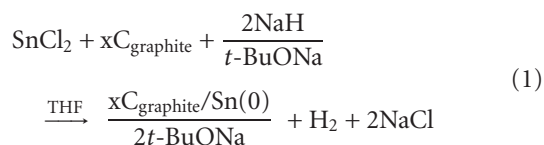
SnO₂, 781 mAhg⁻¹) [2, 3] compared to that of graphite [4, 5]. Lithium can be inserted into tin to form alloys of high Li content up to Li₂₂Sn₅, corresponding to a theoretical capacity of 994 mAhg⁻¹ [2]. Although these attractive features have initiated a number of studies on Sn-based hosts [4, 6–19], Li⁺ ion insertion/extraction into/from Sn causes volume changes [9, 20, 21]. These changes result in cracking and crumbling of the electrode with the concomitant loss of electrical contact both between interparticles, and between particles and the current collector, resulting in poor cycling performance.

A promising way of improving the cyclability of Sn-based electrodes is to synthesize small-sized Sn particles. We have recently developed a new method for the preparation of nanosized Sn particles based on the reduction of tin +2 or +4 chlorides by alkoxide-activated sodium hydride [14, 15]. The discharge capacity of graphite/Sn materials prepared by this method was maintained above ca. 420 mAhg⁻¹ after 15 cycles [16, 19].

In this paper, in order to study the effect of the C/Sn ratio on the electrochemical characteristics of the Sn negative electrode, tin-supported graphite materials were synthesized by reduction of C/SnCl₂ mixtures of various ratios (5, 8, and 12) using the *t*-BuONa-activated NaH chemical reduction process. The structural and morphological changes and electrochemical performances of the materials obtained were studied. All investigations were discussed with respect to unmodified graphite.

2. Experimental

2.1. Synthesis of Graphite/Sn Nanocomposites. The C/Sn materials were prepared by reduction of SnCl₂ by *t*-BuONa-activated NaH in anhydrous THF. Prior to the experiment, NaH was degreased by washing with anhydrous THF under protective nitrogen atmosphere. In a typical experiment, NaH (resp., 41, 61 or 97 mmol for initial C/Sn ratios of 12, 8, and 5) was dispersed in 25 mL THF and the mixture was heated at 65°C under vigorous stirring. *t*-BuOH (resp., 20, 30, or 48 mmol for C/Sn ratios of 12, 8, and 5) was then added dropwise to form the alkoxide-activated hydride *t*-BuONa/NaH. The stirring was continued for 15 min and the mixture was then cooled to room temperature. Graphite (1.44 g) was then added and the mixture was further stirred for 10 min. SnCl₂ (resp., 10, 15, or 24 mmol for C/Sn ratios of 12, 8, and 5) was then added in one portion and the mixture was heated to reflux under constant stirring for 1 h. Hydrogen gas release can be observed, indicating the reduction of SnCl₂ into Sn(0) nanoparticles as presented in



After the reaction had been stopped by cooling down the solution to room temperature, THF and organic volatiles were evaporated under vacuum (40°C, 10 mmHg). The dark grey powder obtained was first dried at room temperature overnight, washed with ethanol (2 × 30 mL) and water (2 × 30 mL) by centrifugation to remove NaCl, the stabilizing alkoxide *t*-BuONa, and unreacted starting materials, and finally dried in vacuum for 12 h (room temperature, 10⁻³ mmHg).

2.2. Materials Characterization. Powder (XRD) analyses were carried out using an automated powder diffractometer with MoK α radiation ($\lambda = 0.709 \text{ \AA}$) (Rotaflex RU-200B, RIGAKU generator and CPS 120 INEL detector, transmission assembly) in capillary mode. Powder was introduced under argon into Lindemann tubes which were further sealed to avoid any pollution. Transmission electron microscopy (TEM) images were taken by placing a drop of the particles in THF onto a carbon film supported copper grid. Samples were studied using a Philips CM20 instrument with LaB₆ cathode operating at 200 kV and equipped with an EDX

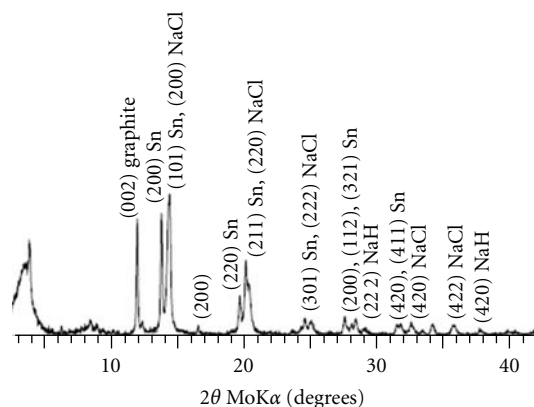


FIGURE 1: XRD patterns of the material prepared with a C/Sn ratio of 8 after synthesis and drying.

(EDAX) spectrometer. A field emission gun-scanning electron microscopy (FEG-SEM Hitachi S2500) equipped with EDX analysis was also used.

2.3. Electrochemical Measurements. Electrochemical tests were carried out in half cells with lithium acting both as reference and counter electrode in 1.5 M LiClO₄-ethylene carbonate (EC). The working electrode was made by coating a 1-methyl-2-pyrrolidinone slurry of 90% w/w of the Sn-based material and 10% w/w of polyvinylidene fluoride (PVDF) on a copper current collector. Charge and discharge cycles were monitored in galvanostatic mode using a Mac Pile potentiostat-galvanostat (Biologic). The output voltage was recorded for a specific current cell of 10 $\mu\text{A}/\text{mg}$ applied for 6 min followed by a 10 s relaxation period.

3. Results and Discussion

3.1. Structure of the C/Sn Materials. In order to gain insights into the chemical composition and into the atomic ratio of Sn/C in the composites after purification, as-prepared and washed samples were first submitted to elemental analyses. For the as-prepared materials and after subtraction of the carbon associated to the stabilizing *t*-BuONa alkoxide, chemical analyses afforded C/Sn ratios in good accordance with those expected when starting with initial C/Sn ratios of 12, 8, and 5. The atomic percentage of tin removed during the washing process was found to be high, quite 70% for the 3 composites prepared. After washing, C/Sn ratios determined by elemental analyses were of 42, 24, and 16, respectively, for materials prepared with initial C/Sn ratios of 12, 8, and 5 (Table 1).

The phase and purity of the powder samples prepared were first determined by X-ray diffraction (XRD). A typical diffraction pattern of the material prepared with a C/Sn ratio of 8 before washing is shown in Figure 1. For the as-synthesized nanocomposite, the diffraction peaks at low angles ($<10^\circ$) were characteristic of the organic *t*-BuONa matrix used to stabilize the tin nanoparticles [22]. All the other reflections of the crude sample could be readily

TABLE 1: Reversible theoretical and experimental capacities of the C/Sn = 42, C/Sn = 24, and C/Sn = 16 nanocomposites.

| Materials composition | | | Reversible capacities calculated from elemental analyses (mAhg ⁻¹) | | | Reversible capacities calculated from electrochemical curves (mAhg ⁻¹) | | |
|-----------------------|--------------------------------------|----------|--|----------|-----|--|----------|-----|
| Initial C/Sn ratio | Experimental C/Sn ratio ^a | | Total | Graphite | Tin | Total | Graphite | Tin |
| 12 | 42 | Cycle 1 | 453 | 279 | 175 | 455 | 285 | 170 |
| | | Cycle 20 | 453 | 279 | 175 | 478 | 321 | 157 |
| 8 | 24 | Cycle 1 | 497 | 260 | 237 | 430 | 228 | 202 |
| | | Cycle 20 | 497 | 260 | 237 | 420 | 240 | 180 |
| 5 | 16 | Cycle 1 | 550 | 208 | 342 | 450 | 243 | 207 |
| | | Cycle 20 | 550 | 208 | 342 | 428 | 245 | 182 |

^aDetermined from elemental analysis.

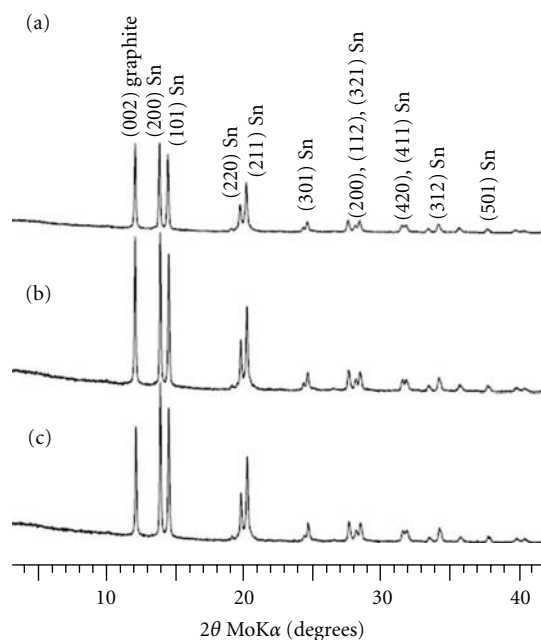


FIGURE 2: XRD patterns of the nanocomposites with C/Sn ratios of (a) 42, (B) 24, and (c) 16, after washing with ethanol and water and drying.

assigned to metallic β -Sn (JCPDS No 04-0673) and to sodium chloride, present as a byproduct of the reduction. For β -Sn, all reflections correspond to the $I4_1/amd$ space group ($a = b = 5.831 \text{ \AA}$, $c = 3.182 \text{ \AA}$, $\alpha = \beta = \gamma = 90^\circ$). A small peak at around 16.8° can be associated to the residual sodium hydride in the crude reaction product.

Peaks related to sodium chloride, sodium hydride, and to the organic matrix disappeared after washing with ethanol and water, and the final nanocomposites with C/Sn ratios of 42, 24, and 16 showed only the reflections of β -Sn and of graphite (strong (002) diffraction line, d_{002} , at ca. 12°) (Figure 2). No crystalline impurities related to reaction by-products or to crystalline tin oxides were detected for the powders after washing.

Further investigations of Sn/graphite nanocomposites were performed by transmission electron microscopy (TEM) and scanning electron microscopy (SEM). Using TEM, it was

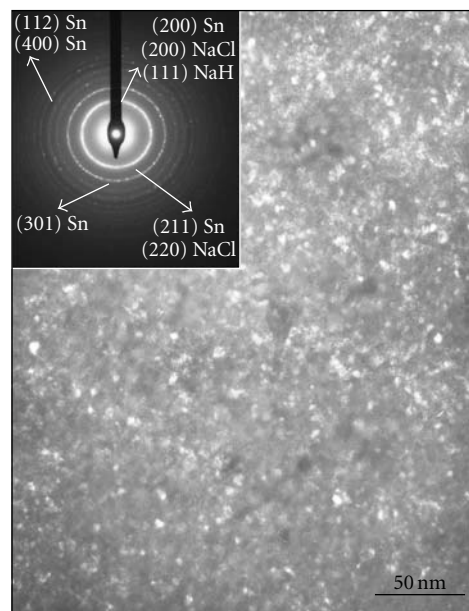


FIGURE 3: Typical TEM micrograph of the as-prepared graphite/tin nanocomposites before washing. The inset is the selected area electron diffraction of the material showing crystalline characteristics of β -Sn.

observed that Sn particles obtained after synthesis and drying have sizes well below 10 nm (Figure 3). They are spherically shaped, show a homogeneous distribution with an average diameter of 5.5 nm, and exhibit the diffraction rings of β -Sn.

Upon washing with ethanol and water, nanometer-sized Sn particles coalesce and aggregate into larger particles due to the removal of the stabilizing t -BuONa ligand. Regardless of the C/Sn ratio, TEM micrographs (Figures 4(a)–4(c)) show that Sn is present as aggregates (with lengths up to 250 nm) composed of spherical particles with diameters ranging from 10 to 50 nm. The corresponding selected-area electron diffraction (SAED) patterns show clear ring patterns confirming the formation of polycrystalline C/Sn materials. The diffraction rings from inside to the outside of the pattern can be indexed to the (200), (101), (220), (321), (312), and (521) planes of quadratic β -Sn, respectively. These results are in good accordance with those of the previous XRD studies.

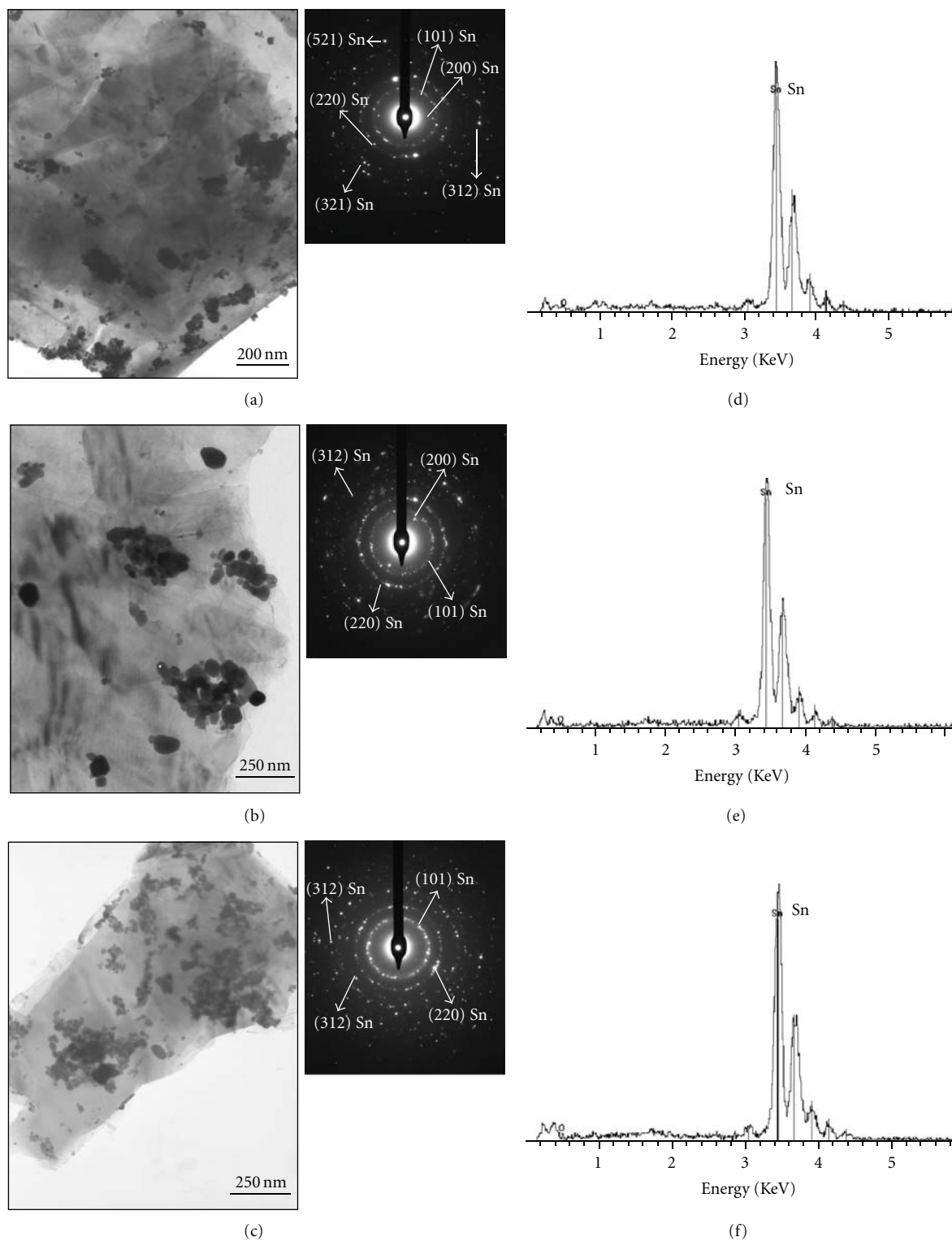


FIGURE 4: TEM images, selected area electron diffraction patterns (SAED), and associated EDS spectra of Sn/graphite nanocomposites after washing with ethanol and water. (a) and (d) C/Sn = 42; (b) and (e) C/Sn = 24; (c) and (f) C/Sn = 16.

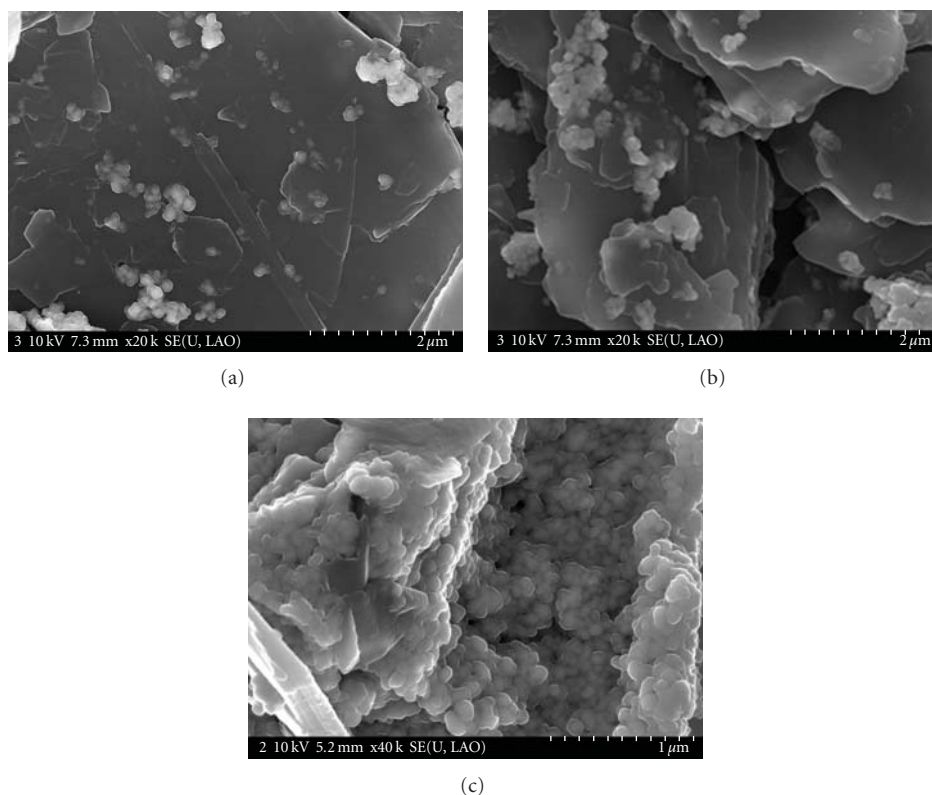


FIGURE 5: SEM micrographs of the Sn/graphite nanocomposites; (a) C/Sn = 42, (b) C/Sn = 24, and (c) C/Sn = 16.

The energy dispersive X-ray spectra (EDX) depicted in Figures 4(d)–4(f) performed on particles aggregates suggest the existence of Sn and O in the washed materials. Elemental analyses derived from EDX spectra show that the weight percentage of O associated to Sn varies between 0 and 7% depending on the particles observed. Using TEM, it was finally observed that Sn particles are located at the edge of graphite layers and at the surface of graphite regardless of the nanocomposite.

Scanning electron microscopy (SEM) observations confirmed the microstructure of Sn particles after purification (Figure 5). All composites contain large Sn aggregates (up to 300 nm) composed of smaller Sn particles possessing an average diameter of ca. 50 nm, which is in accordance with TEM observations. The amount of agglomerated Sn increased with the content of metal in the composite material. Large aggregates with lengths up to 4 μm nonhomogeneously distributed at the surface of graphite layers could clearly be observed for the material with a C/Sn ratio of 16 (Figure 5(c)). Graphite layers provide a limited number of active surface sites for Sn particles anchorage. The formation of the large particles for the C/Sn = 16 material could be a consequence of the high metal content of this composite where metal particles are not adequately stabilized.

3.2. Electrochemical Properties of the C/Sn Materials. To evaluate the potential applicability in Li-ion batteries, we investigated some electrochemical characterizations of the

Sn/graphite composites with respect to Li insertion/extraction. Figure 6 shows a comparison of the voltage profiles of C/Sn washed materials with C/Sn ratios of 42, 24, and 16. Figure 7 and Table 1 summarize the reversible and irreversible theoretical and experimental capacities of the 3 samples.

For the C/Sn = 42 material, the full capacity is of 1145 $\text{mAh}\cdot\text{g}^{-1}$ during the first reduction. 700 $\text{mAh}\cdot\text{g}^{-1}$ are due to irreversible losses related to the reduction of the tin oxidized species and to the formation of the Solid Electrolyte Interphase (SEI) passivation layer at the surface of graphite and on tin particles. Tin oxides SnO and SnO₂ are reduced between 1.8 V and 1.5 V versus Li⁺/Li, respectively. One observes on the first cycle a beginning of reduction towards 1.8 V which continues until 0.8 V and which extends on a relatively large range of capacities (approximately 220 $\text{mAh}\cdot\text{g}^{-1}$). The reduction of tin oxides (Sn⁺⁴, Sn⁺² were evidenced by recent Mossbauer studies [23]) present in our composite can thus be estimated to be ca. 10 $\text{mAh}\cdot\text{g}^{-1}$. Side reactions with products composing the matrix surrounding the Sn nanoparticles should also be considered taking into account that the composite contains ca. 7.5 wt% of these materials according to elemental analysis. Around 0.8–0.6 V versus Li⁺/Li, the formation of the passivation layer (reduction of electrolytic species) occurs. The insoluble products thus generated precipitate at the surface of graphite and tin nanoparticles forming an impermeable film to the solvent molecules but allowing the diffusion of Li⁺ cations. The irreversible capacity related to graphite during

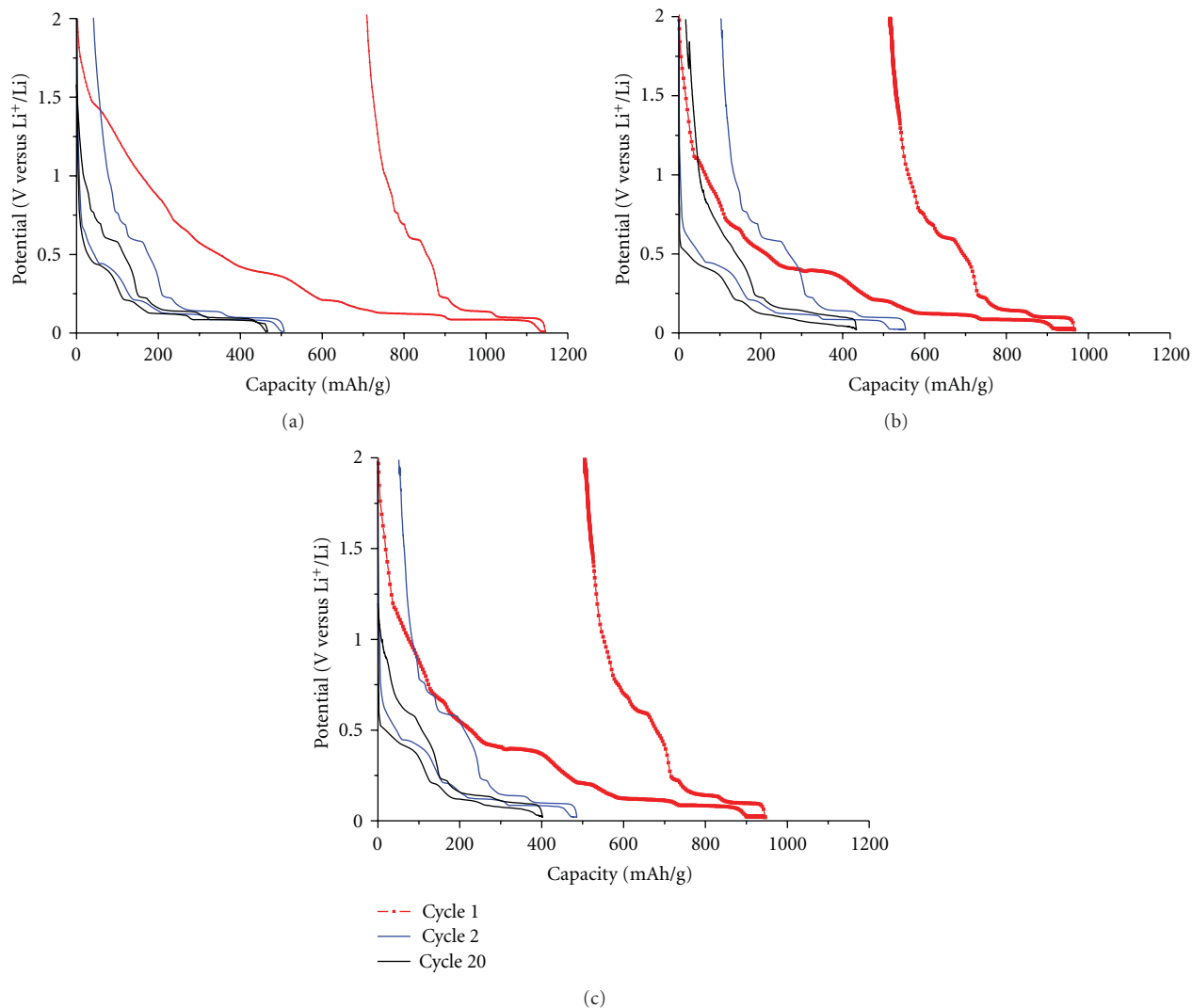


FIGURE 6: Voltage profiles of the (a) $C/Sn = 42$, (b) $C/Sn = 24$, and (c) $C/Sn = 16$ materials cycled between 0 and 2.0 V. The 1st, 2nd, and 20th cycles have been reported for further comparison.

the formation of this passivation layer can be estimated to be ca. $100 \text{ mAh}\cdot\text{g}^{-1}$. The $380 \text{ mAh}\cdot\text{g}^{-1}$ remaining can form the SEI on tin. The irreversible capacity decreases very quickly ($30 \text{ mAh}\cdot\text{g}^{-1}$ at the second cycle) and disappears at the third cycle.

At the first cycle, the reversible capacity is $455 \text{ mAh}\cdot\text{g}^{-1}$, in which $285 \text{ mAh}\cdot\text{g}^{-1}$ can be attributed to graphite and $170 \text{ mAh}\cdot\text{g}^{-1}$ are related to tin. In the second cycle, the reversible capacity increases notably and reaches $478 \text{ mAh}\cdot\text{g}^{-1}$ ($321 \text{ mAh}\cdot\text{g}^{-1}$ for graphite and $157 \text{ mAh}\cdot\text{g}^{-1}$ for tin). This reversible capacity remains stable until the 20th cycle. During the first two cycles, the reversible capacity related to graphite increases by 12% (from 285 to $321 \text{ mAh}\cdot\text{g}^{-1}$). We suppose that, during the synthesis, graphite undergoes small structural disorders which prevent it from cycling at its maximal value during the first cycles. In the meantime, the reversible capacity related to tin decreases by 8% (from 170 to $157 \text{ mAh}\cdot\text{g}^{-1}$). This decrease can originate from the loss of electrical contact between

tin(0) particles formed by the reduction of the oxidized tin species during the first cycle. Indeed, these particles are surrounded by Li_2O , by-product of the reduction, which is a bad electronic conducting material [4, 24]. The formation of large particles and/or aggregates, which behave like massive tin, can also be hypothesized.

A theoretical reversible capacity can be calculated using the values obtained from elemental analyses. The value obtained is $453 \text{ mAh}\cdot\text{g}^{-1}$, in which $279 \text{ mAh}\cdot\text{g}^{-1}$ can be attributed to UF_4 graphite and $175 \text{ mAh}\cdot\text{g}^{-1}$ related to tin. The values of experimental capacities related to graphite and tin suppose that there is no covering between the end and the beginning of the insertion of lithium in tin and graphite. Of course, actually there exists a small zone of potential where the two processes take place simultaneously. Thus the values indicated above for the share of reversible capacity related to tin and to graphite are very slightly underestimated for tin and on the contrary overestimated for graphite.

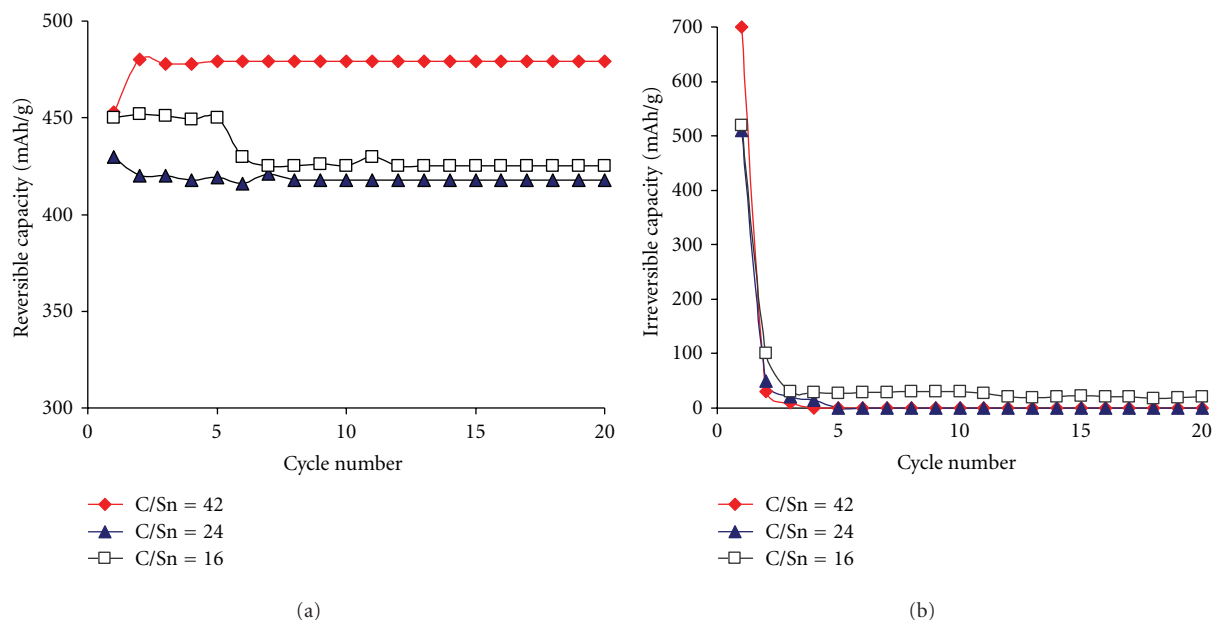


FIGURE 7: Evolution of (a) the reversible and (b) the irreversible capacities of the $C/Sn = 42$, $C/Sn = 24$, and $C/Sn = 16$ materials versus cycle number.

The electrochemical behaviour of the samples containing larger amounts of tin ($C/Sn = 24$ and $C/Sn = 16$) is close to that obtained for the $C/Sn = 48$ material. One can however note that the reversible capacities are slightly lower throughout the 20 cycles and that irreversible capacities persist upon cycling around $30 \text{ mAh}\cdot\text{g}^{-1}$. Table 1 shows finally that during the first cycle, a considerable part of tin is electrically isolated and does not cycle (20% and 40%, respectively, for $C/Sn = 24$ and $C/Sn = 16$ nanocomposites, calculated using elemental analysis values and with the first cycle voltage profiles).

4. Conclusion

In summary, we have demonstrated that the solution phase reduction process using *t*-BuONa-activated NaH in THF can be successfully used for the preparation of tin particles dispersed on graphite. A comparison of the electrochemical behaviour of the materials obtained using C/Sn ratios of 42, 24, and 16 revealed that, despite the high irreversible capacity observed for the theoretical $C/Sn = 42$ nanocomposite at the first cycle, this material exhibits a high reversible capacity of ca. $480 \text{ mAh}\cdot\text{g}^{-1}$ over 20 cycles, that is higher by 37% than the practical expected for pure graphite ($350 \text{ mAh}\cdot\text{g}^{-1}$). This result might be related to the improved dispersion of Sn nanoparticles at the surface of graphite in this composite compared to materials prepared with C/Sn ratios 24 or 16 as demonstrated by TEM and SEM characterizations. Our study shows that the C/Sn ratio used for the preparation of tin/graphite composites is of great importance for obtaining good cycling performances and thus for the development of Sn/graphite systems which could be used as anode materials for Li-ion batteries.

References

- [1] J.-M. Tarascon and M. Armand, "Issues and challenges facing rechargeable lithium batteries," *Nature*, vol. 414, no. 6861, pp. 359–367, 2001.
- [2] M. Winter and J. O. Besenhard, "Electrochemical lithiation of tin and tin-based intermetallics and composites," *Electrochimica Acta*, vol. 45, no. 1-2, pp. 31–50, 1999.
- [3] G. Derrien, J. Hassoun, S. Panero, and B. Scrosati, "Nanostructured Sn-C composite as an advanced anode material in high-performance lithium-ion batteries," *Advanced Materials*, vol. 19, no. 17, pp. 2336–2340, 2007.
- [4] Y. Idota, T. Kubota, A. Matsufuji, Y. Maekawa, and T. Miyasaka, "Tin-based amorphous oxide: a high-capacity lithium-ion-storage material," *Science*, vol. 276, no. 5317, pp. 1395–1397, 1997.
- [5] E. Kim, D. Son, T.-G. Kim et al., "Mesoporous/crystalline composite material containing tin phosphate for use as the anode in lithium-ion batteries," *Angewandte Chemie International Edition*, vol. 43, no. 44, pp. 5987–5990, 2004.
- [6] M. Winter, J. O. Besenhard, M. F. Spahr, and P. Novak, "Insertion electrode materials for rechargeable lithium batteries," *Advanced Materials*, vol. 10, no. 10, pp. 725–763, 1998.
- [7] R. A. Huggins, "Lithium alloy negative electrodes," *Journal of Power Sources*, vol. 81-82, no. 1-2, pp. 13–19, 1999.
- [8] J. Yang, M. Wachtler, M. Winter, and J. O. Besenhard, "Sub-microcrystalline Sn and Sn-Sb powders as lithium storage materials for lithium-ion batteries," *Electrochemical and Solid-State Letters*, vol. 2, no. 2–4, pp. 161–163, 1999.
- [9] L. Y. Beaulieu, S. D. Beattie, T. D. Hatchard, and J. R. Dahn, "The electrochemical reaction of lithium with tin studied by in situ AFM," *Journal of the Electrochemical Society*, vol. 150, no. 4, pp. A419–A424, 2003.
- [10] A. Trifonova, M. Winter, and J. O. Besenhard, "Structural and electrochemical characterization of tin-containing graphite compounds used as anodes for Li-ion batteries," *Journal of Power Sources*, vol. 174, no. 2, pp. 800–804, 2007.

- [11] S.-H. Ng, S.-Y. Chew, D. I. Dos Santos et al., "Hexagonal-shaped tin glycolate particles: a preliminary study of their suitability as Li-ion insertion electrodes," *Chemistry—An Asian Journal*, vol. 3, no. 5, pp. 854–861, 2008.
- [12] P. Meduri, C. Pendyala, V. Kumar, G. U. Sumanasekera, and M. K. Sunkara, "Hybrid tin oxide nanowires as stable and high capacity anodes for Li-ion batteries," *Nano Letters*, vol. 9, no. 2, pp. 612–616, 2009.
- [13] K. Ui, S. Kikuchi, Y. Kadoma, N. Kumagai, and S. Ito, "Electrochemical characteristics of Sn film prepared by pulse electrodeposition method as negative electrode for lithium secondary batteries," *Journal of Power Sources*, vol. 189, no. 1, pp. 224–229, 2009.
- [14] L. Balan, R. Schneider, D. Billaud, and J. Ghanbaja, "Novel low-temperature synthesis of tin(0) nanoparticles," *Materials Letters*, vol. 59, no. 8-9, pp. 1080–1084, 2005.
- [15] L. Balan, R. Schneider, D. Billaud, and J. Ghanbaja, "A new organometallic synthesis of size-controlled tin(0) nanoparticles," *Nanotechnology*, vol. 16, no. 8, pp. 1153–1158, 2005.
- [16] L. Balan, J. Ghanbaja, P. Willmann, and D. Billaud, "Novel tin-graphite composites as negative electrodes of Li-ion batteries," *Carbon*, vol. 43, no. 11, pp. 2311–2316, 2005.
- [17] L. Balan, R. Schneider, J. Ghanbaja, P. Willmann, and D. Billaud, "Electrochemical lithiation of new graphite-nanosized tin particle materials obtained by SnCl_2 reduction in organic medium," *Electrochimica Acta*, vol. 51, no. 17, pp. 3385–3390, 2006.
- [18] D. Billaud, L. Balan, R. Schneider, and P. Willmann, "The influence of the synthesis conditions of graphite/tin nanoparticle materials on their electrode electrochemical performance in Li-ion battery anodes," *Carbon*, vol. 44, no. 12, pp. 2508–2515, 2006.
- [19] L. Balan, R. Schneider, P. Willmann, and D. Billaud, "Tin-graphite materials prepared by reduction of SnCl_4 in organic medium: synthesis, characterization and electrochemical lithiation," *Journal of Power Sources*, vol. 161, no. 1, pp. 587–593, 2006.
- [20] I. A. Courtney and J. R. Dahn, "Electrochemical and in situ X-ray diffraction studies of the reaction of lithium with tin oxide composites," *Journal of the Electrochemical Society*, vol. 144, no. 6, pp. 2045–2052, 1997.
- [21] A. Sivashanmugara, T. P. Kumar, N. G. Renganathan, S. Gopukumar, M. Wohlfahrt-Mehrens, and J. Garche, "Electrochemical behavior of Sn/SnO₂ mixtures for use as anode in lithium rechargeable batteries," *Journal of Power Sources*, vol. 144, no. 1, pp. 197–203, 2005.
- [22] C. Nabais, R. Schneider, C. Bellouard, J. Lambert, P. Willmann, and D. Billaud, "A new method for the size- and shape-controlled synthesis of lead nanostructures," *Materials Chemistry and Physics*, vol. 117, no. 1, pp. 268–275, 2009.
- [23] C. Mercier, R. Schneider, D. Billaud, J. C. Jumas, and J. Olivier-Fourcade, manuscript in preparation.
- [24] K. Wan, S. F. Y. Li, Z. Gao, and K. S. Siow, "Tin-based oxide anode for lithium-ion batteries with low irreversible capacity," *Journal of Power Sources*, vol. 75, no. 1, pp. 9–12, 1998.